BILINGUAL PUBLISHING GROUP

Journal of Atmospheric Science Research

Volume 6 • Issue 3 • July 2023 ISSN 2630-5119(Online)

Volume 6 Issue 3 • July 2023 • ISSN 2630-5119 (Online)

Journal of Atmospheric Science Research

BILINGUAL PUBLISHING GROUP

BILINGUAL PUBLISHING GROUP

Volume 6 | Issue 3 | July 2023 | Page1-51

Journal of Atmospheric Science Research

Contents

Articles

20 **Variation of Dynamical Parameters with Upper Tropospheric Potential Vorticity in Tropical Cyclone over the North Indian Ocean Using WRF Model**

A.H.M. Fazla Rabbi, Ishtiaque M. Syed, Md. Abdullah Elias Akhter, M A K Mallik

30 **Relationship and Variability of Atmospheric Precipitation Characteristics in the North-West of Ukraine**

Svetlana Vasilievna Budnik

41 **Air Pollution Risk Assessment Using GIS and Remotely Sensed Data in Kirkuk City, Iraq**

Huda Jamal Jumaah, Abed Jasim, Aydin Rashid, Qayssar Ajaj

Review

1 **Role of Different Moisture Sources in Driving the Western Himalayan Past-glacier Advances**

Prachita Arora, Sheikh Nawaz Ali, Anupam Sharma

BILINGUAL PUBLISHING GROUP

Journal of Atmospheric Science Research

https://journals.bilpubgroup.com/index.php/jasr

REVIEW

Role of Different Moisture Sources in Driving the Western Himalayan Past-glacier Advances

***Prachita Arora*[1,2], *Sheikh Nawaz Ali*[1,2*], *Anupam Sharma*[1]**

[1] *Birbal Sahni Institute of Palaeosciences, Lucknow, 226007, India*

[2] *Academy of Scientific and Innovative Research, Ghaziabad, 201002, India*

ABSTRACT

The fragmented pattern and the rapidly declining preservation of older glacial features/evidences limits the precision, with which glacial chronologies can be established. The challenge is exacerbated by the scarcity of datable material and limitations of dating methods. Nevertheless, the preserved glacial landforms have been fairly utilized to establish glacial chronologies from different sectors of the Indian Himalayas. The existing Himalayan glacial chrono-stratigraphies have revealed that in a single valley, past glacial advances rarely surpass four stages. Thus, local and regional glacial chronologies must be synthesized to understand glacial dynamics and potential forcing factors. This research presents an overview of glacier responses to climate variations revealed by glacial chrono-stratigraphies in the western Indian Himalayan region over the Quaternary (late). The synthesis demonstrated that, although the glacial advances were sporadic, glaciers in western Himalayas generally advanced during the Marine isotope stage (MIS)-3/4, MIS-2, late glacial, Younger Dryas (YD) and Holocene periods. The Holocene has witnessed multiple glacial advances and the scatter is significant. While previous glacial research revealed that Himalayan glaciers were out of phase with the global last glacial maximum (gLGM), weak Indian Summer Monsoon (ISM) has been implicated (ISM was reduced by roughly 20%). Recent research, however, has shown that gLGM glaciation responded to the global cooling associated with the enhanced mid-latitude westerlies (MLW). Further, the magnitude of gLGM glacier advance varied along and across the Himalayas particularly the transitional valleys located between the ISM and MLW influence. It is also evident that both the ISM and MLW have governed the late Quaternary glacial advances in the western Himalayan region. However, the responses of glaciers to ISM changes are more prominent. The insights gained from this synthesis will help us understand the dynamics of glacier response to climate change, which will be valuable for future climate modelling.

Keywords: Glacial chrono-stratigraphy; Dating technique limits; Climate drivers; Western Himalaya; India

*CORRESPONDING AUTHOR:

Sheikh Nawaz Ali, Birbal Sahni Institute of Palaeosciences, Lucknow, 226007, India; Academy of Scientific and Innovative Research, Ghaziabad, 201002, India; Email: snawazali@gmail.com

ARTICLE INFO

Received: 30 March 2023 | Revised: 09 May 2023 | Accepted: 15 May 2023 | Published Online: 25 May 2023

DOI: https://doi.org/10.30564/jasr.v6i3.5581

CITATION

Arora, P., Ali, S.N., Sharma, A., 2023. Role of Different Moisture Sources in Driving the Western Himalayan Past-glacier Advances. Journal of Atmospheric Science Research. 6(3): 1-19. DOI: https://doi.org/10.30564/jasr.v6i3.5581

1. Introduction

The Himalayan mountain range, which spans eight Asian nations and shelters the most glaciers outside of the Polar regions, is referred to be Asia's "third pole or water tower" [1,2]. The reason is that the melt water from the snow and glaciers feeds some of the most important river systems that provide freshwater to millions of people in the Indo-Gangetic Plain and Central and East China [2,3]. However, since the little ice age (LIA), a general receding trend of the Himalayan glaciers has been observed, with few exceptions from the Karakoram region, where some glaciers have been reported to be standstill or to be advancing, a phenomenon referred to as the Karakoram anomaly [4-7]. According to recent studies, the rate of melting in the Himalayan region has accelerated over the last four decades, making the situation more worrying [8]. Considering the present trend of glacier melting, it is anticipated that future scenarios would have cascading consequences on mountain hydrology, biodiversity, and ecosystem services [9,10]. Although a precise understanding of the climatic characteristics of mountain regions is crucial, complexity arises from a lack of observational data with an adequate spatial and temporal resolution, particularly in the complex topographic regions, and significant difficulty in representing such terrains in current general circulation climate models (GCMs) [11]. Since alternative palaeoclimatic archives, such as lake sequences, are limited and sometimes represent a shorter time frame, the study of past glacial advances in the Himalayan region becomes increasingly essential.

High mountain glaciers are among the most sensitive and best recorders of climate change due to their propensity to respond to the combined effects of snowfall and temperature changes [12-14]. The entire Himalayan ecosystem, including glaciers, has responded to climate change; however, because this region is so vast and diverse—including variations in climate (temperature and precipitation)—it is extremely difficult to comprehend the dynamics of glaciers at different time scales across the region. As a result, understanding and determining the impact of diverse climatic conditions on glacier dynamics across the Himalayas will be challenging until and unless extensive data sets of past changes are compiled from various catchments. During the past two decades, glacial chronologies have been developed in several sectors of the Indian Himalayas, notably the western and central Himalayas. However, the palaeoclimatic patterns and the timing of past glaciations, in particular, remain controversial not only for the tropical/monsoonal sectors of the Himalayas [15], but also for the entire Indian Himalayan region, owing to the vast environmental diversity and geographical vibrancy of the region [16].

The Indian summer monsoon (ISM) and the mid-latitude westerlies (MLW) are the two principal precipitation sources that feed the Himalayas and the Himalayan glaciers from a climatological standpoint. The influence of these two weather systems on the glacial dynamics of the Himalayas is highly complicated and yet to be thoroughly investigated. In addition, the timing and extent of glacier oscillations are poorly known over the majority of the Himalayas and Tibet. In recent years, a great deal of effort and attention has been devoted to this region, especially with the aid of new remote-sensing techniques and numerical dating methods such as optically stimulated luminescence (OSL) and terrestrial cosmogenic radio-nuclide (TCN) surface exposure dating, which have provided new insights into the nature of Pleistocene and Holocene glacial oscillations [3,17-20].

As mentioned before glaciers respond to the combined effects of precipitation (snowfall) and temperature [13]; however, glaciers in low precipitation areas are more susceptible to precipitation changes, whereas glaciers in high precipitation regions are more sensitive to temperature changes [13,14,21]. Established chronologies (mainly exposure ages) indicate that glaciers, particularly in the MLW-dominated north-western Himalaya (Ladakh and Karakoram), appear to have gained mass (advanced) during times of enhanced insolation and ISM as well as enhanced MLW phases [16], although the exact mechanisms of glacier advances are still unclear. Given the lack of chronological data and the complexity mentioned above, the present

research is an attempt to analyze the glacial chronologies established in various sectors of the western Himalaya and to comprehend the mechanisms responsible for driving the glacier advances.

2. Study area

The present synthesis and review of the past glacier advances (phases/stages) of the western Himalayan region include the state of Himachal Pradesh and the two union territories; Jammu and Kashmir and Ladakh of India (**Figure 1**). The majority of the land area of this region shelters the mountains and experiences moderate to scanty summer rainfall (ISM) and is also contributed by the winter snowfall (MLW), which is the primary source of glacier sustenance at the current time.

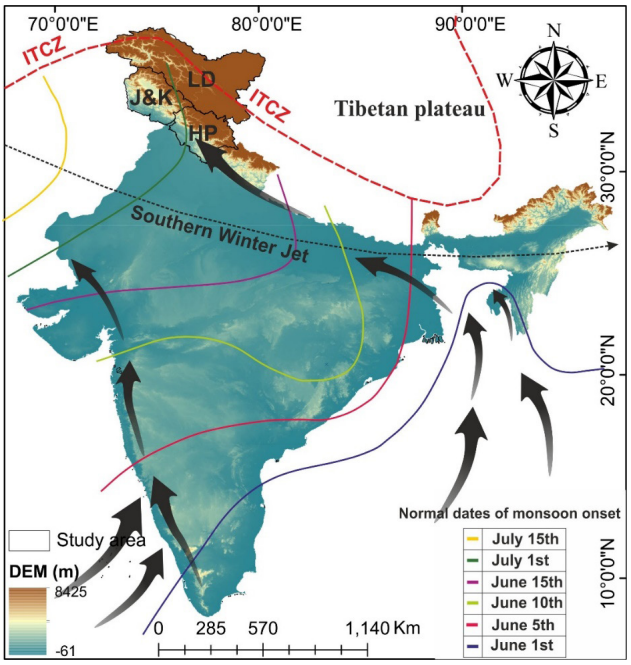

Figure 1. Shuttle Radar Topography Mission (SRTM) digital elevation model (DEM) showing the trajectories of two major weather systems viz. the Indian summer monsoon and the mid-latitude westerly along with the onset of monsoon in different parts of India. The red (dash) line shows the position of summer The Inter-Tropical Convergence Zone (ITCZ).

The high mountain areas (above 3000 m asl) of this region comprise snow-clad peaks, glaciated valleys, glaciers and alpine meadows. The Ladakh Batholith and Palaeozoic to Cretaceous sediments, meta-sediments, granitic intrusions, make up the majority of the area [22]. Climatologically, the two primary weather systems (ISM and MLW) nourish the glaciers in such a way that the MLW strongly influences the glaciers in the western Himalayas during the winter season (December to February), while the ISM governs/nourishes the glaciers in the eastern and central Himalayas [16,23,24]. The current glacier chronology synthesis is focused on the western Himalayan region, which is influenced by both summer ISM and winter MLW precipitation. As a result, the research area extends from the Chandra valley in the east (Himachal Pradesh) to the Nubra-Shyok valley in the west, Ladakh (**Figure 2**).

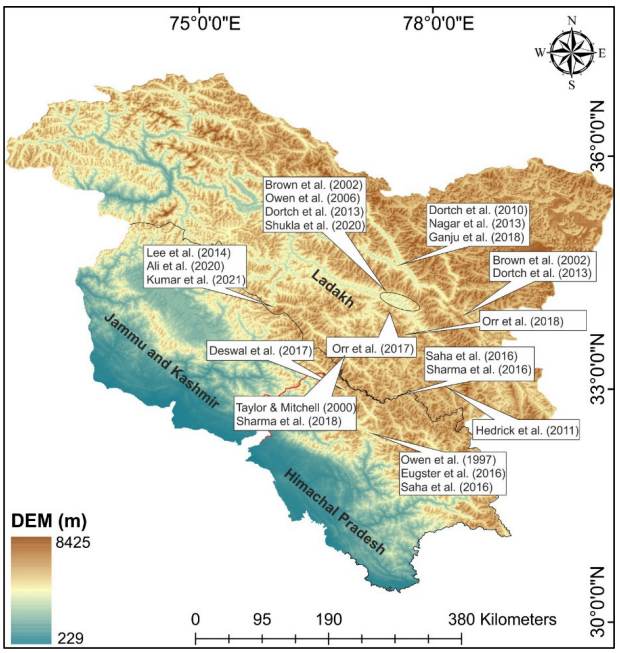

Figure 2. Shuttle Radar Topography Mission (SRTM) digital elevation model (DEM) showing the elevation ranges and the locations of various palaeo-glacial (chrono-stratigraphic) studies from the western and north western Indian Himalayan region.

The semi-arid to arid high altitude terrain of the western Himalayas is referred to "cold desert" due to the scanty rainfall which is attributed to a steady decline in ISM rainfall from east to west/northwest. This decline in the precipitation is ascribed to the Higher Himalayan ranges which act as a barrier and prevent the propagation of moisture laden ISM winds further northward [24-26]. Owing to the low precipitation and hence the low erosional rates, the landforms created by past glacier advances (moraines) are better preserved in this region (**Figure 3**).

Figure 3. Field photographs showing some well-preserved lateral moraines and the largest glacier (Drang-Drung Glacier) in the Zanskar valley, Western Himalaya.

3. Methodology

To understand the palaeoclimatic history of the western Himalayas and the response of glaciers to the major driving factors in the region as a whole, twenty-three (23) previously published research papers on past glacial reconstructions from the region (**Figure 4**) that showed moisture conditions and the response of glacier to the major weather systems (ISM and MLW) during the last 450 ka were synthesized. **Figure 4** depicts a time-series breakdown of the glacier advances documented in the palaeoclimatic data for the western Himalayan region. Here we have used the inferred span of the glacial stages rather than the probability reconstructed on the basis of individual moraine ages. In this way, the synthesis is largely based on the inferences of individual studies and the staking gives a general idea about the synchrony of various glacial advances in this region. These glacial chronologies are predominantly based on optically stimulated luminescence (OSL) and cosmogenic radionuclide (CRN) dating techniques. **Table 1** gives an overview of fundamental information pertaining to the study, such as the location, dating method, and temporal range of these aforementioned palaeoclimatic records. It should be noted that the usage of the question mark "?" in the table implies a lack of chronology for the distinct phases.

Besides synthesizing the glacial records as per the inferences drawn in the available glacial records, we have also used all the reported ages of the moraines to develop a probability density function (PDF). The higher probability shows that the glacier advances were predominant and hence reported in a number of studies. Hence the higher PDF would imply that the glaciers have synchronously responded to the contemporary climatic conditions since the past 450 ka (**Table 1** and **Figure 5**). Here the probability density function (PDF) determines the probability of glacier advances and the values range from 0 to 1. It is estimated in the current study using the NORMDIST, or normal distribution tool. The NORMDIST function

Table 1. Established glacial chronologies using radiocarbon, luminescence and CRN exposure dating techniques from the western Himalayas, India.

S.No.	Location	Glacial Stage					Dating method	Reference
1.	Lahaul Himalaya	Chandra glacial stage (?)	Batal glacial stage (60-45 ka)	Kulti glacial stage (29-10 ka)	Sonapani-I glacial stage (7.5-2.5 ka)	Sonapani-II glacial stage (0.4-0.3 ka)	OSL	Owen et al. [70]
2.	Zanskar Range		Chandra glacial Stage (?)	Batal glacial Stage (78-40 ka)	Kulti glacial Stage (22-8 ka)	Sonapani glacial Stage (0.4-0.3 ka)	OSL	Taylor and Mitchell [64]
3.	Tangste valley (Leh)					Moraine age (105-75 ka; MIS-4)	CRN	Brown et al. [21]
4.	Ladakh Range	Indus valley glacial Stage (> 430ka)	Leh stage (200-130 ka)	Kar stage (105-80 ka)	Bazgo stage (74-41 ka)	Khalling stage (10-6 ka)	CRN	Owen et al. [30]
5.	Nubra-Shyok valley			Deshkit 3 (157-107 ka)	Deshkit 2 (87-75 ka)	Deshkit 1 (49-45 ka)	CRN	Dortch et al. [35]
6.	Southern Zanskar Range (Puga valley)		PM-0 stage (131-107 ka)	PM-1 stage (55-36 ka)	PM-2 stage (7.6-2.1 ka)	PM-3 stage (1.2-0.2 ka)	CRN	Hedrick et al. [31]
7.	Southern Zanskar Range (Karzok valley)	KM-0 stage (314-306 ka)	KM-1 stage KM-2 stage KM-3 stage (72 ± 31 ka)			KM-4 stage (3.6 ± 1.1 ka)	CRN	Hedrick et al. [31]
8.	Ladakh Range	Ladakh-4 glacial stage (100-60 ka)	Ladakh-3 glacial stage	Ladakh-2 glacial stage (25-19 ka)	Ladakh-1 glacia l stage (22-2 ka)	Ladakh Cirque glacial stage (2.2-1.4 ka)	CRN	Dortch et al. [46]
9.	Pangong Range			Pangong-2 glacial stage (105-70 ka)	Pangong-1 glacial stage (43-37 ka)	Pangong Cirque glacial stage (0.7-0.1 ka)	CRN	Dortch et al. [46]
10.	Nubra Valley			Khimi 1/10 (24.0 ± 2 ka)		TIRIT 1/10 (18 ± 1.0 ka)	OSL	Nagar et al. [85]
11.	Nun-Kun massif	Achambur glacial stage (62.7-38.7 ka) (MIS-4 - 3)	Tongul glacial stage (17.4-16.7 ka)	Amantick glacial stage (14.3 ka; 12.4-11.7 ka)	Lomp glacial stage dated to the Little Ice Age (0.5-0.4 ka)	Tanak glacial stage (recent)	CRN	Lee et al. [65]
12.	Chandra Valley					CVG (20 ka)	CRN	Eugster et al. [18]
13.	Yunam valley		79 to 52 ka	17-15 ka	9-7 ka	1.4-1 ka	CRN	Saha et al. [73]

Table 1 continued

S.No.	Location	Glacial Stage					Dating method	Reference
14.	Zanskar Range (Sarchu Plain)			Sarchu Glaciation Stage-1 (MIS-4)	Sarchu Glaciation Stage-2 (22-19 ka)	Sarchu Glaciation Stage-3 (8.2 ka cooling event)	OSL	Sharma et al. [44]
15.	Lahaul Himalaya			Miyar stage (pre-gLGM)	Khanjar stage (10-6 ka)	Menthosa Advance (LIA) 0.3-0.2 ka	OSL	Deswal et al. [74]
16.	Gopal Kangri valley		MG (124-78 ka)	MG (33-24 ka)	MG (37-12 ka)	MG (1.5-1 ka)	CRN	Orr et al. [36]
17.	Stok Kangri valley		MS4 38.7 ± 6.6 ka)	MS3 (16 ± 2.4 ka)	MS2 (0.6 ± 0.2 ka)	MS1 (1.2 ± 0.3 ka)	CRN	Orr et al. [36]
18.	Nubra valley		(Tirith-II) 60.4 ± 5.2 ka (MIS-4)	(Tirith-I) 30 ± 2.5 ka beginning of MIS-2	Third minor glacial advance 6.8 ± 1.0/7.2 ± 1.4 ka	Youngest stage (1.0 ± 0.4 ka)and (0.5 ± 0.2 ka)	OSL	Ganju et al. [19]
19.	Lato massif, Zanskar Range			Lato glacial stage (244-49 ka)	Shiyul glacial stage (25-15 ka)	Kyambu glacial stage (3.4-0.2 ka)	CRN	Orr et al. [32]
20.	Southern Zanskar Range		Southern Zanskar Glacier Stage-4 (MIS-4)	Southern Zanskar Glacier Stage-3 (24-17 ka)	Southern Zanskar Glacier Stage-2 (17-13 ka)	Southern Zanskar Glacier Stage-1 (5-4 ka)	OSL	Sharma and Shukla [45]
21.	Suru valley					Tongul glacier stage (24 to 20 ka; gLGM)	OSL	Ali et al. [86]
22.	Southern Ladakh Range (Puche valley)			PGA-I (35-29 ka)	PGA-II (15-13 ka)	PGA-III (?/Holocene)	OSL	Shukla et al. [55]
23.	Suru Valley	Suru-I (33-23 ka)	Suru-II (17-15 ka)	Suru-III (13-11 ka)	Suru-IV (10-7.3 ka)	Suru-V (2.8-2.3 ka)	OSL	Kumar et al. [20]

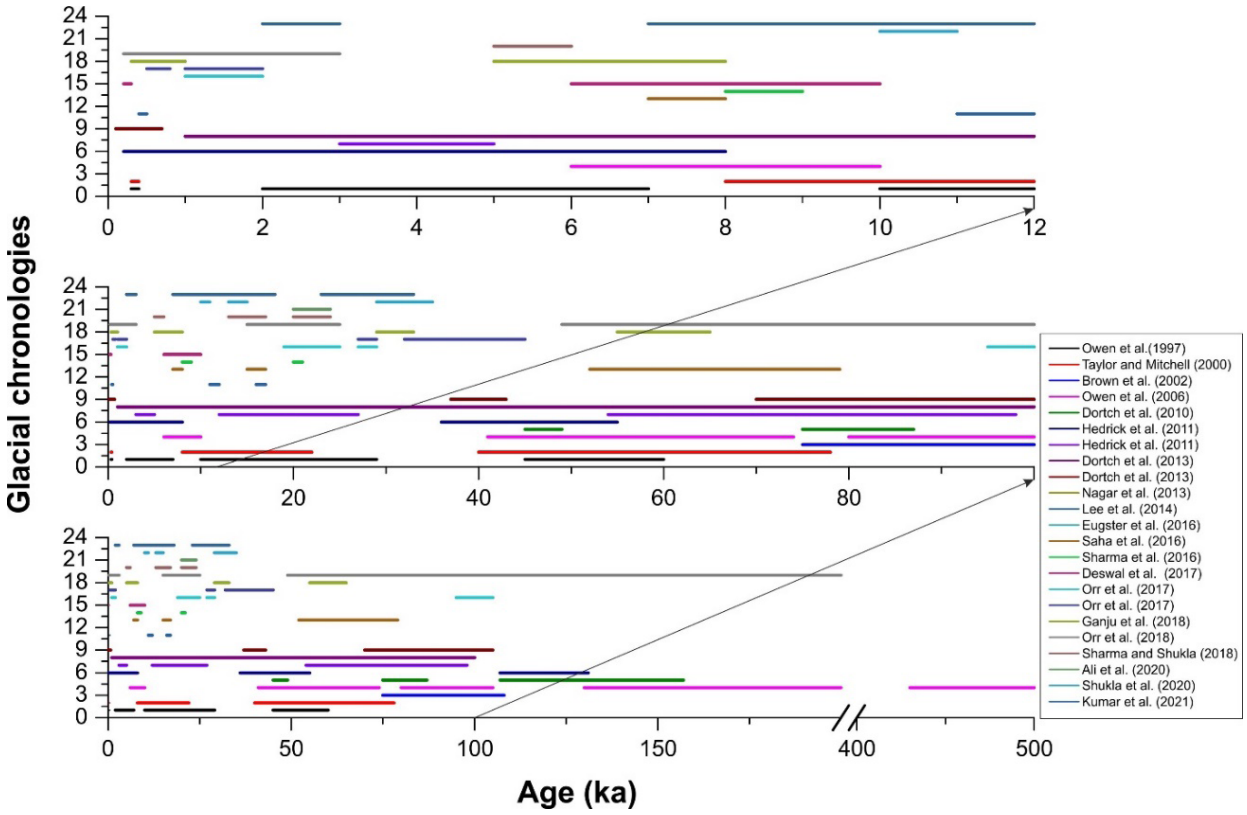

Figure 4. OSL and CRN derived chronologies of the glacial advances in the western Himalayas, India on three different timescales.

takes four arguments: The X-value, the mean, the standard deviation, and the cumulative value. Each X-value is calculated once the mean and standard deviation have been determined. The cumulative value is also set to "false", enabling the function to produce the normal probability density. After calculating a PDF for each X-value, it is plotted against the timing of glacier advances. To visually enhance the PDF peaks, each value is multiplied by its associated age. For a more precise regional correlation, PDF was created for moraine ages up to 100 ka as well (**Figure 5**). In addition, for each study, an age rank plot was created to show the distribution of ages (with errors), arranged in ascending order. The objective was to visualize any patterns or trends in the age distribution.

It is to be noted that each study's description of moisture (precipitation) conditions is qualitative, and the nomenclature is highly generic. Since both OSL and CRN dating methods have been used for establishing the chronologies, a general comparison of the two is necessary (explained in the following section).

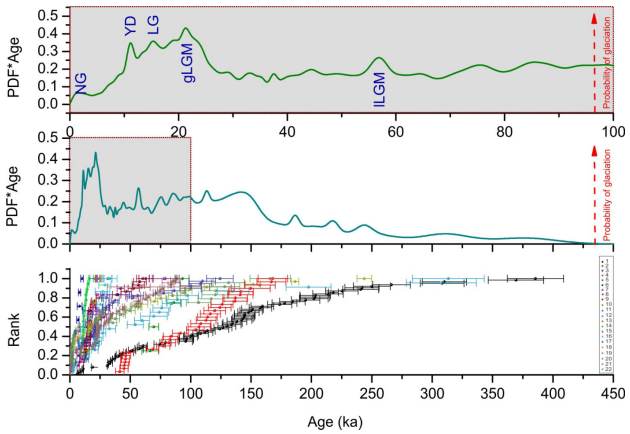

Figure 5. Moraine ages of the past glacier advances and the Gaussian probability density function to represent the probability of glacier advances over the western Himalayas along with the rank plot (bottom) showing the distribution of the chronologies from the western Himalayas used in the study: 1). Owen et al. [30], 2). Dortch et al. [35], 3). Taylor and Mitchell [64], 4). Ali et al. [86], 5). Brown et al. [21], 6). Deswal et al. [74], 7). Eugester et al. [18], 8). Ganju et al. [19], 9). Lee et al. [65], 10). Sharma and Shukla [45], 11). Shukla et al. [55] 12). Sharma et al. [44], 13). Rothlisberger and Geyh [89], 14). Owen et al. 2001, 15). Saha et al. 2016, 16). Kumar et al. [20], 17). Orr et al. [36], 18). Orr et al. [32], 19). Nagar et al. [85], 20). Dortch et al. [46], 21). Hedrick et al. [31] (Puga) 22). Hedrick et al. [31] (Karzok).

Therefore, to quantify the precipitation information associated with ISM and westerlies, inferences drawn from the 23 palaeo-glacial (climatic) records rather than the reported ages, were used to synthesize the palaeoclimatic data. For the cluster analysis using TILIA, the phases/events/stages that reported a glacial advance were assigned a weightage of 10, while the remaining ages were assigned a weightage of 0.1 (**Figures 6 and 7**). The platform TILIA was originally designed for the storage, analysis and display of palaeoecological data. One of its analytical tools CONISS carries out stratigraphically constrained cluster analysis in order to group variables into zones to facilitate better description and correlation. The analysis is done by using the method of incremental sum of squares and although the method was initially intended for stratigraphic data, it has been found useful for other types of linearly ordered data as well and thus used in the present study. For more details on cluster analysis using TILIA, please see Grimm, 1987 [27].

In order to get a better understanding of the role of different weather systems (ISM/MLW), the PDF form using the published ages was correlated with the regional and global palaeoclimatic archives. This is because these archives are direct/indirect indicators of ISM/MLW intensities. Such correlations can provide useful insights into the complex interactions between various climate processes and give insights regarding the response and drivers of past glacier changes.

4. Results and discussion

In high mountain regions, where biotic proxies are generally scarce or discontinuous and of shorter durations, the glaciers offer the potential to reconstruct past climate due to their sensitivity to ever-changing temperature and precipitation [3,14]. Understanding past climate change through glacial responses can provide valuable information in simulations for futuristic climatic simulations (models). Over the past few decades, various researchers have made use of well-preserved glacier landforms in reconstructing the past glacier changes in order to decipher the complexities of the driving mechanisms of such glaciations as well as understand their synchrony in the topographically and climatologically

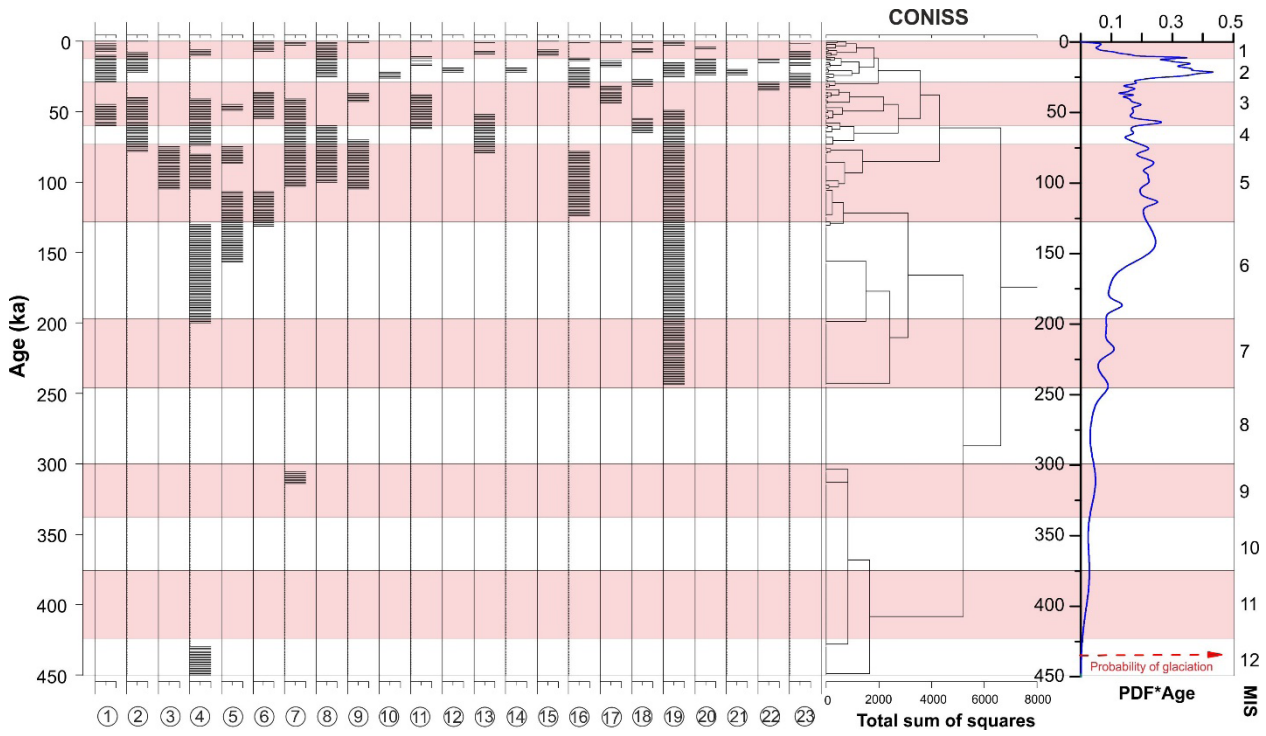

Figure 6. Cluster analysis of glacier advances constructed using TILIA is plotted against the Gaussian probability density function (PDF) to represent the probability of glacier advances over the western Himalayas.

complex Himalayan region. Thus synthesizing the available glacial chronological datasets enables us to identify broad trends in climatic variability over the region and correlations between the glacial chronological datasets and past climatic records lays the foundation for reliable future climate model simulations (**Figures 4-6**). Keeping this in view, the present study attempts to provide a comprehensive analysis of Late Quaternary climate of westerly dominated Indian Himalaya based on a compilation of 23 available (**Figures 6 and 7**) palaeoclimate records.

The results and discussions are divided into two sections: The MLW-dominated NW Himalaya and the transitional climatic zone impacted by both ISM and MLW.

4.1 Chronologies from NW Himalaya

It has been observed that the oldest records of glaciation are available from the northwestern (NW) region (**Figures 4 and 5**) of the Indian Himalayas and very slow erosional rates may be implicated [28,29]. The slow erosion driven preservation of these records can be attributed to the region's climate, which is characterized by low summer rainfall (being in the rain-shadow zone), resulting in less erosion and hence the preservation of landforms for longer time scales. The oldest and most extensive glacial advance in this region is reported from the Ladakh Range and has been named as 'Indus valley glacial stage' (**Figures 4 and 5**). Terrestrial cosmogenic radio-nuclide surface exposure dating (CRN) of the preserved moraine boulders assigned this stage to be 430 ka [30]. From the Zanskar Himalaya, the first and oldest glacial stage reported is KM-0, which is dated beyond 300 ka [31] (Karazok valley), corresponding tentatively to MIS-9/10 (**Figures 2 and 6**). The climatic correlations of these glacial advances are difficult, since these glacial advances do not provide an absolute age bracket for the glacial advance.

Chronologically, the subsequent glacier advance has been reported from the Ladakh range and based on the clustering of ages between ca. 200 and 130 ka, the moraines of the 'Leh stage' have been assigned the penultimate glacial cycle—MIS 6 [30]. In the Zanskar valley, another older glacier advance (Lato glacial stage) preserved within the Lato massif is dated between MIS 8-3 (244-49 ka) [32], but has a very huge age spread (**Table 1**; **Figures 4 and 5**). The spread in the ^{10}Be ages prevents this stage to be statistically correlated with the other regional stages as well as with other climatic records. During the late MIS-6 and early MIS-5, different glacial advances were observed in the northwestern Himalayas that coincided with the period of intensified ISM [16,33,34]. These included the Deshkit 3 stage (145 ± 12 ka) from Nubra valley [35], the PM-0 stage (131-107 ka) from Puga valley [31], and the MG4 stage (124-78 ka) from Gopal Kangri [36]. Another glacier advance of a relatively lesser extent has been recorded in the Ladakh range (Kar glacial stage); however, due to a wide spread in the ages, it has been assigned to the last glacial cycle (MIS-5) [30]. While there is significant glacial evidence (advance) indicating Himalayan glaciers expanded during the MIS-6 and early MIS-5 glaciations, there is no general agreement on the timing, extent, and climatic forcing of these (especially MIS-6) glacier stages/advances throughout the Himalayan mountain system [37]. Yet, it is possible that these glacial records reflect the penultimate glacial maximum (140 ka), which is in phase with the Northern Hemisphere ice sheets [38,39]. Additionally, ISM precipitation induced by insolation has been suggested to be the primary determinant of such glacier advances throughout the Himalayas [3,40,41]. Taking this into account, it has been hypothesized that, on a regional scale, the MIS-6 glacier advances correspond with the coldest phase and are so advanced as a result of cold climatic conditions and limited melting [40]. Even so, because of the large age range, the primary driving factor (temperature versus precipitation) cannot be precisely defined and requires additional studies, wherein a definite age bracket for such glacier advances can be established.

Dortch et al. [35] identified another 81 ka glacier advance (Deshkit 2) in the Nubra-Shyok valley (where present-day precipitation is governed by MLW), which corresponded with the late MIS-5 to

early MIS-4 glaciations, which were mostly recorded from monsoon-dominated regions (**Figures 6-8**). Moreover, two glacial advances, Ladakh-4 (81 ± 20 ka) and Pangong glacial stage-2 (85 ± 15 ka), were documented from the Ladakh and Pangong ranges. These glacial advances have been found to coincide with the negative $\delta^{18}O$ excursions of the Guliya ice core as well as more negative speleothem $\delta^{18}O$ values from the Sanbao cave indicating an increase in monsoon strength during the early-mid MIS-5 [37,42,43]. The strengthening was immediately followed by a cold trough of late MIS-5 and early MIS 4 corresponding to a period of lower insolation (**Figure 8**).

Glacial advances occurred in several parts of Zanskar during the MIS 4 epoch, including the Sarchu plain (Sarchu glaciation stage-I; MIS 4) [44] and the Southern Zanskar range (SZS-4 stage; MIS-4; **Figures 2 and 4**) [45]. The Bazgo glacial stage, which corresponds to the middle of the last glacial cycle (MIS-3 and/or MIS-4) [30], represents a subsequent glaciation of lesser extent in the Ladakh territory (**Table 1**). Deshkit 1 (45 ka) [35] and Pangong 1 glacial stage (40 ± 3 ka) [46] glacial deposits correlative to the Bazgo stage have been reported in the Nubra Shyok valley. A prominent peak in the probability function (PDF; **Figure 7**) implies that the glacier in the NW Himalayas has advanced during the Mid- MIS-3. This time frame coincides with the prominent negative $\delta^{18}O$ excursions of the NGRIP $\delta^{18}O$ record [47,48], and Guliya ice core [42] (**Figure 8**). On the basis of data presented in **Figure 8**, it is suggested that the mid-MIS-3 glacier advance is a manifestation of amplified mid-latitude westerlies induced by low insolation; as expected in orographic exteriors like the NW Himalayas [43]. Besides the gLGM glacier, there are reports of an early MIS-2 glacier advance [19], which has been ascribed to lower temperatures and a weaker ISM phase. This early MIS-2 cooling has been related to the cooler sea surface temperature resulting in discharging of huge icebergs into north Atlantic Laurentide [49-52]. While the gLGM (19-23 ka) is suggested to be an expression of enhanced MLW associated with lower temperatures [16,18,40,53-55]. Furthermore, it is also suggested that the weaker ISM during the gLGM is a result of enhanced MLW, increased snow accumulation on the Himalayan-Ti-

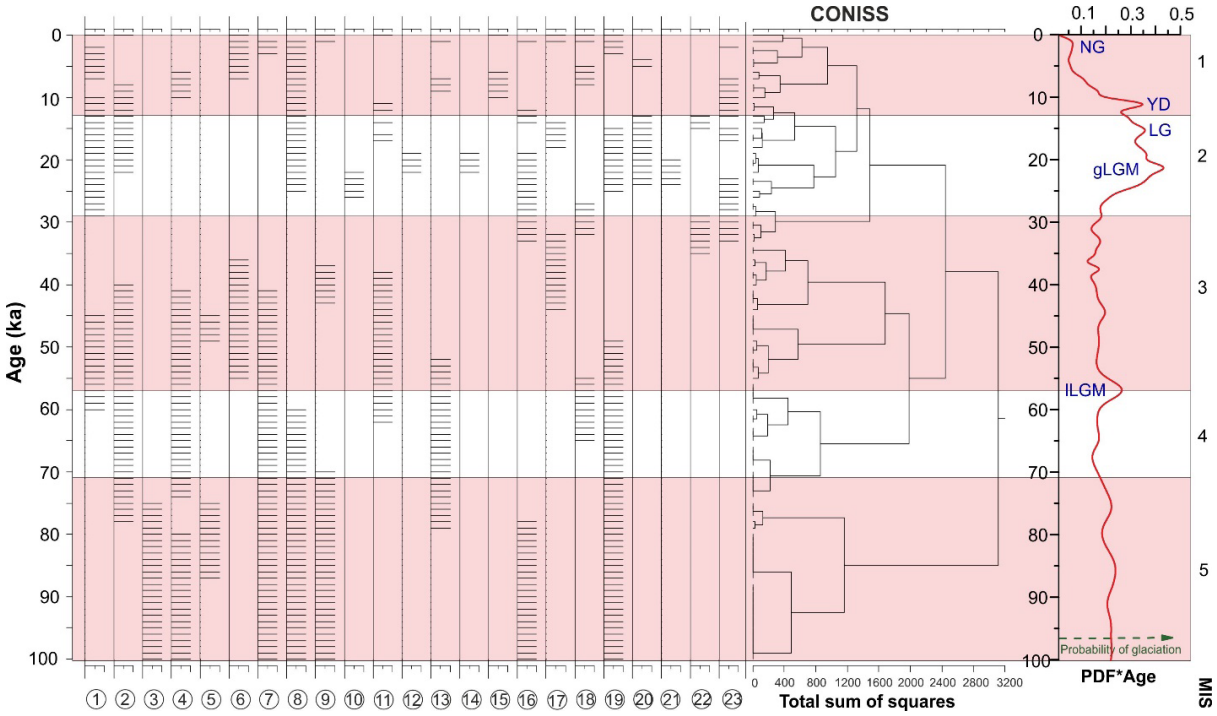

Figure 7. Cluster analysis of glacier advances for last 100 ka plotted against the Gaussian probability density function to represent the probability of glacier advances over the western Himalayas. The pink and white bands show the odd and even marine isotopic stages respectively.

betan orogeny which resulted in the southward shift of the inter-tropical convergence zone (ITCZ) and resulted in a weaker ISM [56-58].

The younger glacial stages of lesser extent, namely Sarchu glaciation stage 2 (Sarchu plain) [49], Shiyul glacial stage (Lato massif) [32], Southern Zanskar glacial stage 3 (Southern Zanskar range) [45], Ladakh 2 glacial stage (Ladakh range) [46], Tirith-I (Nubra Shyok valley) [19] correlate with MIS-2 and constitute the gLGM in this region (**Figure 7**). It has been observed that several glacial advances in the western Himalayas that are contemporaneous with the gLGM are less extensive than prior glacial advances ($_{l}$LGM). These glacial advances, however, are larger than those recorded in the central and eastern Himalayas. Significant negative $\delta^{18}O$ excursions of the NGRIP $\delta^{18}O$ record [47,48], and Guliya ice core [42], suggest enhanced MLW, while less negative values from Speleothem $\delta^{18}O$ records from Bittoo cave (dark green [59]), $\delta^{18}O$ from Hulu (olive [60]), Dongge Cave (orange [31]), suggest a weaker monsoon during low insolation period (**Figure 8**). Given that insolation driven ISM precipitation was much lower during gLGM than the MIS-3 and 1 [62], this likely explains the restricted glacial extent in parts of the NW Himalayas that get moisture primarily from the MLW [16]. This would imply that the glacier in the exterior of the contemporary ISM influence is more sensitive to insolation driven ISM precipitation.

The glacier advances during the late glacial and MIS-1 periods better represent the changes in temperature and precipitation. Small glacier advances in the Southern Zanskar range are indicated by terminal moraines corresponding to SZS-2 that date back to 15.7 ± 1.3 and 14.3 ± 1.3 ka [40]. Late-glacial advances have been documented throughout the Himalayan orogeny, including the NW and Zanskar Himalayas [32,36-65]. On the basis of their correlations with the ice core and speleothem data (**Figure 8**), it has been suggested that these glacier advances correspond to the northern hemisphere cold events. A prominent peak at the late-glacial and Holocene transitional implies that the NW Himalayan glaciers responded sensitively to the YD (13-11 ka) cooling event which is recorded throughout the Himalayan Tibetan orogeny [43,60,66,67]. The YD, a 1300 yr cold event that marked the end of the last deglacial and beginning of the Holocene period (between 12.9-11.7 ka), is linked to the catastrophic release of fresh water from pro-glacial Lake Agassiz and/or the extensive formation of winter sea ice cover, which increased albedo and affected the thermohaline circulation of the Atlantic Ocean [67-69]. Prominent negative values from both NGRIP and Guliya $\delta^{18}O$ records [42,47-48] suggest cooling associated with enhanced MLW and highlight the sensitivity of glaciers to millennial-scale cold events [43,55].

The Southern Zanskar range experienced the youngest glacial advance by mid-Holocene (6 ka), which is linked to a millennial-scale cold event during the enhanced westerlies phase [45]. Siachen Glacial Advance (SGA) is a modest glacial advance dating to the mid-Holocene (6.8 ± 1.0/7.2 ± 1.4 ka) in the Nubra valley [19]. While, in the Lato massif, the Kyambu glacial stage is dated 3.4 ± 0.2 ka, representing the area's youngest stage of glaciation during which glaciers were limited to the massif's cirques and headwalls [32]. The youngest glacier expansion, associated with the Little Ice Age (LIA), is distinguished by snout proximal glacier advance and has been well documented in the Lato massif [32], Ladakh range [46], Nubra valley [19], Pangong range [46], and Nun Kun massif [1-3]. Based on the available data from the NW Himalaya, it is evident that glaciers have sensitively responded and advanced both during the insolation driven intensified ISM and cooler mid-latitude Westerlies [16,40] (**Figures 4-8**).

4.2 Chronologies from W Himalayas

Establishing the timing of glacier advances in Lahaul, W Himalaya was first attempted by Owen et al. [70] using optically simulated luminescence (OSL) and radiocarbon dating techniques. The study suggested that the area has witnessed three glacier advances, namely the 'Chandra Glacial Stage', the 'Batal Glacial Stage', and the 'Kulti Glacial Stage' along with the two minor Holocene advances (**Table 1** and **Figure 4**). OSL dating indicated that the gla-

ciers began to retreat between 43400 ± 10300 and 36900 ± 8400 years ago (during the Batal Stage). The less extensive Kulti Glacial Stage is constrained between 36900 ± 8400 cal years BP during which the glaciers extended 12 km downstream from the contemporary snout. Radiocarbon dating of peat bog revealed basal age of 9160 ± 7014 cal years BP representing a phase of climatic amelioration that was coincident with post-Kulti deglaciation. Therefore, the Kulti glaciation was suggested to be equivalent to parts of late MIS-3, MIS-2, and early MIS-1 respectively. In addition, two minor Holocene advances viz. Sonapani Glacial Stage I (early mid-Holocene) and Sonapani-II glacial advance corresponding to Little Ice Age (LIA) were identified. Later, in another study using the cosmogenic radionuclide dating (^{10}Be and ^{26}Al) technique, Owen et al. [71] provided a more explicit estimate of the timing of individual glacial advances in the Lahaul valley. They could not date the oldest Chandra Glacial Stage, however, Batal Glacial Stage was ascertained to occur at 15.5-12 ka, and has been suggested to be coeval with the Northern Hemisphere Late-glacial Interstadial (Bølling/Allerød). These ages are significantly younger as compared to previously suggested OSL ages of 43.4 ka and 36.9 ka [70,72]. These overestimated OSL ages were attributed to the partial bleaching of the OSL signal. Based on the exposure ages, deglaciation of the Batal Glacial Stage was completed by 12 ka and was followed by a small re-advancement corresponding to the Kulti Glacial Stage during the early Holocene, at 10-11.4 ka (**Figure 6**).

Recently, Eugster et al. [18] revisited the Chandra Valley in the Lahaul region, W Himalaya, and suggested that the trunk of Chandra glacier extended at least up to Udaipur Village (200 km downstream from the present-day glacier snout). Based on their new chronology they suggested that Chandra Valley was occupied by a glacier up to 1000 m thick during the gLGM. However, during the subsequent deglaciation (post 18 ka), the trunk-valley glacier retreated by 70 km and after 15 ka, the main trunk valley must have been mostly ice-free. In this study, they have suggested that the Chandra Valley was occupied by a 1000 m thick and 200 km long glacier and proposed that the LGM glaciation was not restricted in this area and the temperature changes during the LGM controlled the onset of deglaciation [18,72]. This is the first report of such a mega glacier advance from the Himalaya region and a more robust explanation for such an advance is required.

Similarly, glacial advances from the Yunam valley (W Himalaya) were reported using cosmogenic ^{10}Be surface exposure dating [73]. The exposure ages showed that glaciers advanced in this area during the early part of the Last Glacial (79 to 52 ka), and that they may have been coincident with Heinrich events 5 and 6. Another glacier advance was reported to the south of Yunam valley during the Oldest Dryas and/or the Late glacial, 17-15 ka. This time window is also defined by more negative ^{18}O excursions from the Guliya ice core [67] in the current synthesis (**Figures 7-8**). Our findings are supported by the regional glacial stages of Dortch et al. [46], which indicate that this younger glaciation was most likely driven by mid-latitudinal westerlies. The glacier advance that followed was based on exposure ages obtained from boulders inset in drumlins 7.9 ± 1.0 and 6.9 ± 0.9 ka. Based on these findings, it was determined that the main valley glacier advanced before 8-7 ka and that the drumlins and other streamlined landforms originated prior to or during the early Holocene.

Another study from the Lahaul Himalaya identified three stages of glacial advance, of decreasing magnitude and termed, from oldest to youngest, the Miyar stage (MR-I), Khanjar stage (KH-II), and Menthosa advance (M-III). Despite the fact that the oldest Miyar stage could not be dated, it has been suggested to be older than the global Last Glacial Maximum (gLGM) based on the magnitude of the ELA, which is 606 meters. The subsequent glacier advance was constrained between 10-6 ka during the cold Bond event-7 and was sustained beyond the early Holocene climatic optimum. The sustenance was due to the ice-albedo feedback, where an increase in precipitation during the early Holocene was believed to have lowered the summer temperature due to an increase in the cloudiness, and evaporative cooling.

Given the close proximity of the end moraine complex to an ancient human settlement, the third glacier advance has been given the LIA designation, even if the date has not been determined [74].

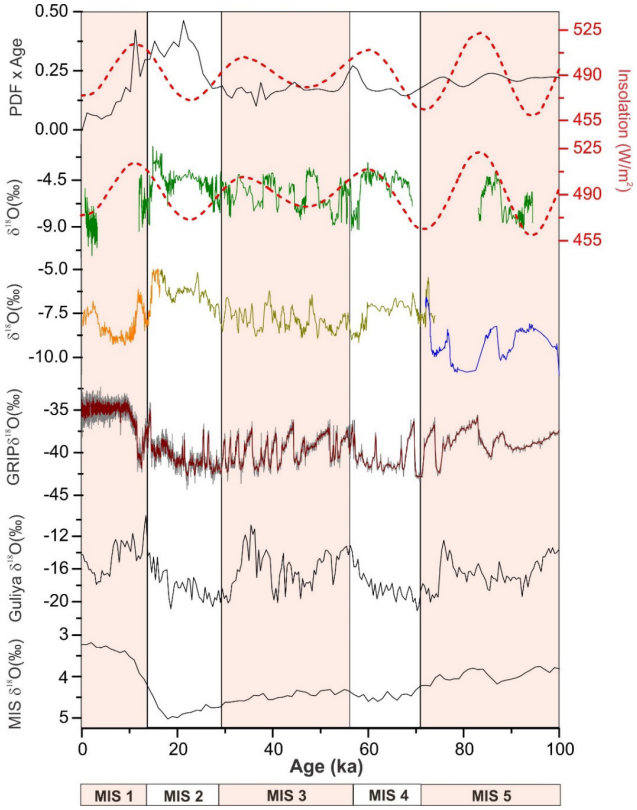

Figure 8. Regional correlation of glacial advances up to 100 ka (overlain by June insolation 30°N data; Berger and Loutre [75]) are compared with the stacked (from the top) Speleothem $\delta^{18}O$ records from Bittoo cave (dark green; Kathayat et al. [59]), $\delta^{18}O$ from Hulu (olive; Wang et al. [60]), Dongge Cave (orange; Yuan et al. [61]), Sanbao Cave (dark blue; Dong et al. [37]), NGRIP $\delta^{18}O$ record from Greenland (Johnsen et al. [47]; Andersen et al. [48]), $\delta^{18}O$ in Guliya ice core (Thompson et al. [42]) and marine $\delta^{18}O$ curve of Lisiecki and Raymo [39] and the simulated monsoon index.

Recent investigations have shown considerable variations in moraine ages using various dating methods. Ganju et al. [19], for example, derived considerably younger optical ages from the Nubra-Shyok valley (NW Himalaya) than Dortch et al. [35] for the three major glacial advances (60.4 ± 5.2 to 42.0 ± 3.0 ka; 30 ± 2.5 to 18.2 ± 1.8 ka; and 7.2 ± 1.4/6.8 ± 1.0 ka). Similar inconsistencies have been found in other studies, emphasizing the need of utilizing at least two dating techniques to cross-check the chronology. These differences in CRN and OSL ages result in different climatic interpretations, which create more uncertainty in comprehending the primary driving mechanisms and climate triggers.

Overall, the dynamics of late Quaternary glacier advances in the western and northwestern Himalayan region reveal a complex interaction among insolation-induced ISM and MLW changes [24,46,75-78]. The available data and inferences suggest that the glaciers have sensitively responded to the enhanced phases of ISM as well as the MLW, however during the enhanced ISM phases the glacier response is more pronounced and may be attributed to the availability of moisture (**Figure 8**). From the present synthesis it can be suggested that during the late MIS-5 and MIS-4, western and northwestern Himalayan region witnessed multiple glacier advances which coincide with the periods of increased insolation (higher ISM) as well as during the low insolation and enhanced mid-latitude westerly phase (MIS 4). Considering that the glaciers in low precipitation are more sensitive to precipitation changes, it is argued that during the increased monsoonal intensity, the ISM moisture laden could have propagated in the region and resulted in the glacier advances. The increased ISM would have resulted in more snowfall at higher altitudes, which could have been assisted by lower temperatures caused by increased cloudiness as well as evaporative cooling [16,24,43,79]. A significant expansion of the glaciers during the gLGM may be attributed to the cooler climate phases associated with the intensified MLW during the MIS-2 [17,43,55,80-87]. The modest glacier advance in this region, compared to the eastern and central Himalayas, is attributed to the geographic location of the area which receives more precipitation from the MLW. The mid-late Holocene glacier advances generally coincide with the enhanced ISM phases and are suggested to be driven by ISM precipitation. Considering that the ISM intensity is generally related to the insolation changes, therefore, the Holocene glacier advances would have required optimal temperature conditions during enhanced ISM phases. As a result of the increased cloud cover, which limits the influx of shortwave

radiation and enhances evaporative cooling, summer temperatures would have been lower and summer snowfall at higher elevations would have been easier [79]. Increased snow and glacier cover produce additional cooling due to the ice-albedo feedback process [66], which likely reduces radiative heating [87].

5. Conclusions

Since high mountain glaciers are sensitive climate probes, they provide both an opportunity and a challenge for understanding past climates and anticipating future changes [3]. Despite the fact that the palaeoclimatic reconstructions of the Himalayan glaciers have been fairly well established, there is still a discrepancy in ages obtained using different dating methods (e.g., OSL vs. CRN vs. radiocarbon). Nevertheless, contrary to previous research that suggested that Himalayan glaciers were out of phase with the global LGM, for which a weak ISM was implicated (ISM was decreased by around 20%), recent research, however, has shown that gLGM glacial responded to the global cooling and showed a modest expansion. Besides that, the extent of gLGM glaciation varied throughout the Himalayas, with transitional valleys (e.g., Chandra valley) seeming to have responded more amply than the westerly dominated NW and ISM dominated central and eastern Himalayas. The age and expansion discrepancies discovered highlight the need for a meticulous and systematic mapping of moraines and other landforms in different climatic zones. Due to the importance of chronometric data in linking stratigraphically constrained deposits with climatic proxies, glacial episodes must be dated using a combination of CRN and OSL dating techniques. It is worth mentioning here that although there is a broad consensus that both the ISM and the mid-latitude Westerlies dictated the pattern of late Quaternary glacial advances in the Himalayan region yet, glacial responses to ISM changes are more apparent. However, the exact mechanisms, timing, and geographical influence of the two weather systems and (a) synchronous response of the glaciers are still being debated. This is large because the influence of these two weather systems varies spatially, i.e. ISM east to west (NW) and MLW NW to south east. Therefore, it's essential to carry out a thorough and systematic investigation of a wide range of landforms (including moraines) from distinct climatic regimes, and to utilize a variety of techniques in combination to establish a reliable chronology.

Author Contributions

SNA, PA and AS conceived the study and developed the overall methodology. PA and SNA reviewed the available data and synthesized it. SNA, PA and AS carried out the writing of the manuscript.

Conflict of Interest

The authors declare that they have no known competing financial interests or personal relationships that could have appeared to influence the work reported in this paper.

Data Availability Statement

Data will be made available on request.

Acknowledgement

The authors are thankful to the Director, Birbal Sahni Institute of Palaeosciences, Lucknow for constant support and providing infrastructural facilities.

References

[1] Immerzeel, W.W., Van Beek, L.P.H., Bierkens, M.F.P., 2010. Climate change will affect the Asian water towers. Science. 328(5984), 1382-1385.

[2] Scott, C.A., Zhang F., Mukherji A., et al., 2019. Water in the Hindu Kush Himalaya. The Hindu Kush Himalaya assessment. Springer: Cham. DOI: https://doi.org/10.1007/978-3-319-92288-1_8

[3] Owen, L.A., 2009. Latest Pleistocene and Holocene glacier fluctuations in the Himalaya and Tibet. Quaternary Science Reviews. 28, 2150-2164.

[4] Haeberli, W., Frauenfelder, R., Hoelzle, M., et al., 1999. On rates and acceleration trends of global glacier mass changes. Geografiska Annaler: Series A, Physical Geography. 81(4), 585-591.

[5] Ageta, Y., Naito, N., Nakawo, M., et al., 2001. Study project on the recent rapid shrinkage of summer-accumulation type glaciers in the Himalayas. Bulletin of Glaciological Research. 18, 45-49.

[6] Hewitt, K., 2005. The Karakoram anomaly? Glacier expansion and the 'elevation effect', Karakoram Himalaya. Mountain Research and Development. 25(4), 332-340.

[7] Gardelle, J., Berthier, E., Arnaud, Y., et al., 2013. Region-wide glacier mass balances over the Pamir-Karakoram-Himalaya during 1999-2011. The Cryosphere. 7(4), 1263-1286.

[8] Maurer, J.M., Schaefer, J.M., Rupper, S., et al., 2019. Acceleration of ice loss across the Himalayas over the past 40 years. Science Advances. 5(6).

DOI: https://doi.org/10.1126/sciadv.aav7266

[9] Buytaert, W., Moulds, S., Acosta, L., et al., 2017. Glacial melt content of water use in the tropical Andes. Environmental Research Letters. 12(11), 114014.

[10] Milner, A.M., Khamis, K., Battin, T.J., et al., 2017. Glacier shrinkage driving global changes in downstream systems. Proceedings of the National Academy of Sciences. 114(37), 9770-9778.

[11] Beniston, M., Diaz, H.F., Bradley, R.S., 1997. Climatic change at high elevation sites: an overview. Climatic Change. 36(3-4), 233-251.

[12] Kääb, A., Chiarle, M., Raup, B., et al., 2007. Climate change impacts on mountain glaciers and permafrost. Global and Planetary Change. 56(1-2), 7-9.

[13] Pratt-Sitaula, B., Burbank, D.W., Heimsath, A.M., et al., 2011. Topographic control of asynchronous glacial advances: A case study from Annapurna, Nepal. Geophysical Research Letters. 38(24).

[14] Zech, R., Zech, M., Kubik, P.W., et al., 2009. Deglaciation and landscape history around Annapurna, Nepal, based on ^{10}Be surface exposure dating. Quaternary Science Reviews. 28(11-12), 1106-1118.

[15] Schaefer, J.M., Oberholzer, P., Zhao, Z., et al., 2008. Cosmogenic beryllium-10 and neon-21 dating of late Pleistocene glaciations in Nyalam, monsoonal Himalayas. Quaternary Science Reviews. 27(3-4), 295-311.

[16] Ali, S.N., Juyal, N., 2013. Chronology of late quaternary glaciations in Indian Himalaya: A critical review. Journal of the Geological Society of India. 82(6), 628-638.

[17] Ali, S.N., Biswas, R.H., Shukla, A.D., et al., 2013. Chronology and climatic implications of Late Quaternary glaciations in the Goriganga valley, central Himalaya, India. Quaternary Science Reviews. 73, 59-76.

[18] Eugster, P., Scherler, D., Thiede, R.C., et al., 2016. Rapid Last Glacial Maximum deglaciation in the Indian Himalaya coeval with midlatitude glaciers: New insights from ^{10}Be-dating of ice-polished bedrock surfaces in the Chandra Valley, NW Himalaya. Geophysical Research Letters. 43(4), 1589-1597.

[19] Ganju, A., Nagar, Y.C., Sharma, L.N., et al., 2018. Luminescence chronology and climatic implication of the late quaternary glaciation in the Nubra valley, Karakoram Himalaya, India. Palaeogeography, Palaeoclimatology, Palaeoecology. 502, 52-62.

[20] Kumar, V., Mehta, M., Shukla, A., et al., 2021. Late Quaternary glacial advances and equilibrium-line altitude changes in a semi-arid region, Suru Basin, western Himalaya. Quaternary Science Reviews. 267, 107100.

[21] Brown, E.T., Bendick, R., Bourles, D.L., et al., 2002. Slip rates of the Karakorum fault, Ladakh, India, determined using cosmic ray exposure dating of debris flows and moraines. Journal of Geophysical Research: Solid Earth. 107(B9), ESE-7.

[22] Madden-Nadeau, A., 2014. Overview of the

Geology of the Himalayas [Internet]. Available from: https://www.geolsoc.org.uk/~/media/shared/documents/Events/Past%20Meeting%20Resources/Himalaya%2014%20Geology%20of%20the%20Himalayas.pdf

[23] Ageta, Y., Higuchi, K., 1984. Estimation of mass balance components of a summer-accumulation type glacier in the Nepal Himalaya. Geografiska Annaler: Series A, Physical Geography. 66(3), 249-255.

[24] Benn, D.I., Owen, L.A., 1998. The role of the Indian summer monsoon and the mid-latitude westerlies in Himalayan glaciation: Review and speculative discussion. Journal of the Geological Society. 155(2), 353-363.

[25] Sharma, A., Phartiyal, B., 2018. Late quaternary palaeoclimate and contemporary moisture source to extreme NW India: A review on present understanding and future perspectives. Frontiers in Earth Science. 6, 150.

[26] Ali, S.N., Agrawal, S., Sharma, A., et al., 2020. Holocene hydroclimatic variability in the zanskar valley, northwestern Himalaya, India. Quaternary Research. 97, 140-156.

[27] Grimm, E.C., 1987. CONISS: a FORTRAN 77 program for stratigraphically constrained cluster analysis by the method of incremental sum of squares. Computers & Geosciences. 13(1), 13-35.

[28] Adams, B., Dietsch, C., Owen, L.A., et al., 2009. Exhumation and incision history of the Lahul Himalaya, northern India, based on (U-Th)/He thermochronometry and terrestrial cosmogenic nuclide methods. Geomorphology. 107(3-4), 285-299.

[29] Burbank, D.W., Bookhagen, B., Gabet, E.J., et al., 2012. Modern climate and erosion in the Himalaya. Comptes Rendus Geoscience. 344(11-12), 610-626.

[30] Owen, L.A., Caffee, M.W., Bovard, K.R., et al., 2006. Terrestrial cosmogenic nuclide surface exposure dating of the oldest glacial successions in the Himalayan orogen: Ladakh Range, northern India. Geological Society of America Bulletin. 118(3-4), 383-392.

[31] Hedrick, K.A., Seong, Y.B., Owen, L.A., et al., 2011. Towards defining the transition in style and timing of Quaternary glaciation between the monsoon-influenced Greater Himalaya and the semi-arid Transhimalaya of Northern India. Quaternary International. 236(1-2), 21-33.

[32] Orr, E.N., Owen, L.A., Saha, S., et al., 2018. Quaternary glaciation of the lato massif, zanskar range of the NW Himalaya. Quaternary Science Reviews. 183, 140-156.

[33] Bookhagen, B., Thiede, R.C., Strecker, M.R., 2005. Late Quaternary intensified monsoon phases control landscape evolution in the northwest Himalaya. Geology. 33(2), 149-152.

[34] Bookhagen, B., Thiede, R.C., Strecker, M.R., 2005. Abnormal monsoon years and their control on erosion and sediment flux in the high, arid northwest Himalaya. Earth and Planetary Science Letters. 231(1-2), 131-146.

[35] Dortch, J.M., Owen, L.A., Caffee, M.W., 2010. Quaternary glaciation in the Nubra and Shyok valley confluence, northernmost Ladakh, India. Quaternary Research. 74(1), 132-144.

[36] Orr, E.N., Owen, L.A., Murari, M.K., et al., 2017. The timing and extent of Quaternary glaciation of Stok, northern Zanskar Range, Transhimalaya, of northern India. Geomorphology. 284, 142-155.

[37] Dong, G., Zhou, W., Xian, F., et al., 2022. Timing and climatic drivers for the MIS 6 glaciation in the central Himalaya: ^{10}Be surface exposure dating of hummocky moraine northwest of Mt. Gang Benchhen, Paiku Gangri. Palaeogeography, Palaeoclimatology, Palaeoecology. 605, 111230.

[38] Colleoni, F., Wekerle, C., Näslund, J.O., et al., 2016. Constraint on the penultimate glacial maximum Northern Hemisphere ice topography (≈ 140 kyrs BP). Quaternary Science Reviews. 137, 97-112.

[39] Lisiecki, L.E., Raymo, M.E., 2005. A Pliocene Pleistocene stack of 57 globally distributed benthic δ^{18}O records. Paleoceanography and

Paleoclimatology. 20(1).

[40] Murari, M.K., Owen, L.A., Dortch, J.M., et al., 2014. Timing and climatic drivers for glaciation across monsoon-influenced regions of the Himalayan-Tibetan orogen. Quaternary Science Reviews. 88, 159-182.

[41] Chevallier, P., Pouyaud, B., Suarez, W., et al., 2011. Climate change threats to environment in the tropical Andes: Glaciers and water resources. Regional Environmental Change. 11, 179-187.

[42] Thompson, L.O., Yao, T., Davis, M.E., et al., 1997. Tropical climate instability: The last glacial cycle from a Qinghai-Tibetan ice core. Science. 276(5320), 1821-1825.

[43] Ali, S.N., Singh, P., Arora, P., et al., 2022. Luminescence dating of late pleistocene glacial and glacio-fluvial sediments in the Central Himalaya, India. Quaternary Science Reviews. 284, 107464.

[44] Sharma, S., Chand, P., Bisht, P., et al., 2016. Factors responsible for driving the glaciation in the Sarchu Plain, eastern Zanskar Himalaya, during the late Quaternary. Journal of Quaternary Science. 31(5), 495-511.

[45] Sharma, S., Shukla, A.D., 2018. Factors governing the pattern of glacier advances since the Last Glacial Maxima in the transitional climate zone of the Southern Zanskar Ranges, NW Himalaya. Quaternary Science Reviews. 201, 223-240.

[46] Dortch, J.M., Owen, L.A., Caffee, M.W., 2013. Timing and climatic drivers for glaciation across semi-arid western Himalayan-Tibetan orogen. Quaternary Science Reviews. 78, 188-208.

[47] Johnsen, S.J., Clausen, H.B., Dansgaard, W., et al., 1997. The $\delta^{18}O$ record along the Greenland Ice Core Project deep ice core and the problem of possible Eemian climatic instability. Journal of Geophysical Research: Oceans. 102(C12), 26397-26410.

[48] Andersen, K.K., Svensson, A., Johnsen, S.J., et al., 2006. The Greenland ice core chronology 2005, 15-42 ka. Part 1: Constructing the time scale. Quaternary Science Reviews. 25(23-24), 3246-3257.

[49] Heinrich, H., 1988. Origin and consequences of cyclic ice rafting in the northeast Atlantic Ocean during the past 130,000 years. Quaternary Research. 29(2), 142-152.

[50] Bond, G., Heinrich, H., Broecker, W., et al., 1992. Evidence for massive discharges of icebergs into the North Atlantic ocean during the last glacial period. Nature. 360(6401), 245-249.

[51] Bond, G., Broecker, W., Johnsen, S., et al., 1993. Correlations between climate records from North Atlantic sediments and Greenland ice. Nature. 365(6442), 143-147.

[52] Liu, S., Ye, W., Chen, M.T., et al., 2021. Millennial-scale variability of Indian summer monsoon during the last 42 kyr: Evidence based on foraminiferal Mg/Ca and oxygen isotope records from the central Bay of Bengal. Palaeogeography, Palaeoclimatology, Palaeoecology. 562, 110112.

[53] Mix, A.C., Bard, E., Schneider, R., 2001. Environmental processes of the ice age: Land, oceans, glaciers (EPILOG). Quaternary Science Reviews. 20(4), 627-657.

[54] Bali, R., Ali, S.N., Agarwal, K.K., et al., 2013. Chronology of late Quaternary glaciation in the Pindar valley, Alaknanda basin, Central Himalaya (India). Journal of Asian Earth Sciences. 66, 224-233.

[55] Shukla, T., Mehta, M., Jaiswal, M.K., et al., 2018. Late Quaternary glaciation history of monsoon-dominated Dingad basin, central Himalaya, India. Quaternary Science Reviews. 181, 43-64.

[56] Overpeck, J., Anderson, D., Trumbore, S., et al., 1996. The southwest Indian Monsoon over the last 18000 years. Climate Dynamics. 12, 213-225.

[57] Sirocko, F., Garbe-Schönberg, D., McIntyre, A., et al., 1996. Teleconnections between the subtropical monsoons and high-latitude climates during the last deglaciation. Science. 272(5261), 526-529.

[58] Kudrass, H.R., Hofmann, A., Doose, H., et al.,

2001. Modulation and amplification of climatic changes in the Northern Hemisphere by the Indian summer monsoon during the past 80 ky. Geology. 29(1), 63-66.

[59] Kathayat, G., Cheng, H., Sinha, A., et al., 2016. Indian monsoon variability on millennial-orbital timescales. Scientific Reports. 6(1), 1-7.

[60] Wang, Y.J., Cheng, H., Edwards, R.L., et al., 2001. A high-resolution absolute-dated late Pleistocene monsoon record from Hulu Cave, China. Science. 294(5550), 2345-2348.

[61] Yuan, D., Cheng, H., Edwards, R.L., et al., 2004. Timing, duration, and transitions of the last interglacial Asian monsoon. Science. 304(5670), 575-578.

[62] Prell, W.L., Kutzbach, J.E., 1987. Monsoon variability over the past 150,000 years. Journal of Geophysical Research: Atmospheres. 92(D7), 8411-8425.

[63] Rupper, S., Koppes, M., 2010. Spatial patterns in Central Asian climate and equilibrium line altitudes. IOP Conference Series: Earth and Environmental Science. 9(1), 012009.

[64] Taylor, P.J., Mitchell, W.A., 2000. The Quaternary glacial history of the Zanskar Range, northwest Indian Himalaya. Quaternary International. 65, 81-99.

[65] Lee, S.Y., Seong, Y.B., Owen, L.A., et al., 2014. Late Quaternary glaciation in the Nun-Kun massif, northwestern India. Boreas. 43(1), 67-89.

[66] Colin, C., Kissel, C., Blamart, D., et al., 1998. Magnetic properties of sediments in the Bay of Bengal and the Andaman Sea: Impact of rapid North Atlantic Ocean climatic events on the strength of the Indian monsoon. Earth and Planetary Science Letters. 160(3-4), 623-635.

[67] Alley, R.B., 2000. The Younger Dryas cold interval as viewed from central Greenland. Quaternary Science Reviews. 19(1-5), 213-226.

[68] Brauer, A., Haug, G.H., Dulski, P., et al., 2008. An abrupt wind shift in western Europe at the onset of the Younger Dryas cold period. Nature Geoscience. 1(8), 520-523.

[69] Broecker, W.S., Denton, G.H., Edwards, R.L., et al., 2010. Putting the Younger Dryas cold event into context. Quaternary Science Reviews. 29(9-10), 1078-1081.

[70] Owen, L.A., Bailey, R.M., Rhodes, E.J., et al., 1997. Style and timing of glaciation in the Lahaul Himalaya, northern India: A framework for reconstructing late Quaternary palaeoclimatic change in the western Himalayas. Journal of Quaternary Science: Published for the Quaternary Research Association. 12(2), 83-109.

[71] Owen, L.A., Gualtieri, L.Y.N., Finkel, R.C., et al., 2001. Cosmogenic radionuclide dating of glacial landforms in the Lahul Himalaya, northern India: Defining the timing of Late Quaternary glaciation. Journal of Quaternary Science: Published for the Quaternary Research Association. 16(6), 555-563.

[72] Owen, L.A., Derbyshire, E., Richardson, S., et al., 1996. The Quaternary glacial history of the Lahul Himalaya, northern India. Journal of Quaternary Science: Published for the Quaternary Research Association. 11(1), 25-42.

[73] Saha, S., Sharma, M.C., Murari, M.K., et al., 2016. Geomorphology, sedimentology and minimum exposure ages of streamlined subglacial landforms in the NW Himalaya, India. Boreas. 45(2), 284-303.

[74] Deswal, S., Sharma, M.C., Saini, R., et al., 2017. Late holocene glacier dynamics in the Miyar Basin, Lahaul Himalaya, India. Geosciences. 7(3), 64.

[75] Berger, A., Loutre, M.F., 1991. Insolation values for the climate of the last 10 million years. Quaternary Science Reviews. 10(4), 297-317.

[76] Finkel, R.C., Owen, L.A., Barnard, P.L., et al., 2003. Beryllium-10 dating of Mount Everest moraines indicates a strong monsoon influence and glacial synchroneity throughout the Himalaya. Geology. 31(6), 561-564.

[77] Scherler, D., Bookhagen, B., Strecker, M.R., et al., 2010. Timing and extent of late Quaternary glaciation in the western Himalaya constrained by ^{10}Be moraine dating in Garhwal, India. Quaternary Science Reviews. 29(7-8), 815-831.

[78] Rana, N., Sharma, S., Ali, S.N., et al., 2019. Investigating the sensitivity of glaciers to climate variability since the MIS-2 in the upper Ganga catchment (Saraswati valley), Central Himalaya. Geomorphology. 346, 106854.

[79] Rupper, S., Roe, G., Gillespie, A., 2009. Spatial patterns of Holocene glacier advance and retreat in Central Asia. Quaternary Research. 72(3), 337-346.

[80] Ganopolski, A., Rahmstorf, S., Petoukhov, V., et al., 1998. Simulation of modern and glacial climates with a coupled global model of intermediate complexity. Nature. 391(6665), 351-356.

[81] Herzschuh, U., 2006. Palaeo-moisture evolution in monsoonal Central Asia during the last 50,000 years. Quaternary Science Reviews. 25(1-2), 163-178.

[82] Braconnot, P., Otto-Bliesner, B., Harrison, S., et al., 2007. Results of PMIP2 coupled simulations of the Mid-Holocene and Last Glacial Maximum—Part 1: Experiments and large-scale features. Climate of the Past. 3(2), 261-277.

[83] Mehta, M., Dobhal, D.P., Pratap, B., et al., 2014. Late quaternary glacial advances in the tons river valley, Garhwal Himalaya, India and regional synchronicity. The Holocene. 24(10), 1336-1350.

[84] Bisht, P., Ali, S.N., Shukla, A.D., et al., 2015. Chronology of late Quaternary glaciation and landform evolution in the upper Dhauliganga valley, (Trans Himalaya), Uttarakhand, India. Quaternary Science Reviews. 129, 147-162.

[85] Nagar, Y.C., Ganju, A., Satyawali, P.K., et al., 2013. Preliminary optical chronology suggests significant advance in Nubra valley glaciers during the Last Glacial Maximum. Current Science. 105(1), 96-101.

[86] Ali, S.N., Morthekai, P., Bajpai, S., et al., 2020. Redefining the timing of Tongul glacial stage in the Suru Valley, NW Himalaya, India: New insights from luminescence dating. Journal of Earth System Science. 129, 1-11.

[87] Adams, J., Maslin, M., Thomas, E., 1999. Sudden climate transitions during the Quaternary. Progress in Physical Geography. 23(1), 1-36.

[88] Shukla, A.D., Sharma, S., Rana, N., et al., 2020. Optical chronology and climatic implication of glacial advances from the southern Ladakh Range, NW Himalaya, India. Palaeogeography, Palaeoclimatology, Palaeoecology. 539, 109505.

[89] Rothlisberger, F., Geyh, M.A., 1985. Glacier Variations in Himalayas and Karakorum [Internet]. Available from: https://www.researchgate.net/publication/279603460_Glacier_variations_in_Himalayas_and_Karakorum

BILINGUAL PUBLISHING GROUP

Journal of Atmospheric Science Research
https://journals.bilpubgroup.com/index.php/jasr

ARTICLE

Variation of Dynamical Parameters with Upper Tropospheric Potential Vorticity in Tropical Cyclone over the North Indian Ocean Using WRF Model

***A.H.M. Fazla Rabbi*[1*], *Ishtiaque M. Syed*[1], *Md. Abdullah Elias Akhter*[2], *M A K Mallik*[3]**

[1] *Department of Physics, University of Dhaka, Dhaka, 1000, Bangladesh*
[2] *Department of Physics, Khulna University of Engineering and Technology, Khulna, 9208, Bangladesh*
[3] *Bangladesh Meteorological Department, Agargaon, Dhaka, 1207, Bangladesh*

ABSTRACT

Meteorologists are experiencing many challenges in the reliable forecasting of the track and intensity of tropical cyclones (TC). Uses of the potential vorticity (PV) technique will enrich the current forecasting system. The use of PV analysis of TC intensification over the North Indian Ocean (NIO) is rare. In this study, the authors analyze the behaviour of upper-level PV with dynamic parameters of TCs over NIO. The authors used NCEP FNL reanalysis 1 × 1 degree data as input in WRF model version 4.0.3 with one-way nesting between the parent and child domains. The authors used a coupling of the Kain-Fritsch (new Eta) scheme and the WSM 6-class graupel scheme as cumulus and microphysics options to run the model. The authors found that at least one potential vorticity unit (PVU) (1 PVU = 10^{-6} $m^2s^{-1}KKg^{-1}$) upper PV is required to maintain the intensification of TC. Larger upper PV accelerates the fall of central pressure. The high value of upper PV yields the intensification of TC. The wind shear and upper PV exhibited almost identical temporal evolution. Upper PV cannot intensify the TCs at negative wind shear and shear above the threshold value of 12 ms^{-1}. The upper PV and geopotential heights of 500 hPa change mutually in opposite trends. The upper PV calculated by the model is comparable to that of ECMWF results. Therefore, the findings of this study are admissible.

Keywords: Dynamic; Vorticity; Geopotential; WRF; Tropical and intensification

*CORRESPONDING AUTHOR:
A.H.M. Fazla Rabbi, Department of Physics, University of Dhaka, Dhaka, 1000, Bangladesh; Email: rabbiphy@gmail.com

ARTICLE INFO
Received: 10 May 2023 | Revised: 11 July 2023 | Accepted: 18 July 2023 | Published Online: 25 July 2023
DOI: https://doi.org/10.30564/jasr.v6i3.5717

CITATION
Fazla Rabbi, A.H.M., Syed, I.M., Akhter, M.A.E., et al., 2023. Variation of Dynamical Parameters with Upper Tropospheric Potential Vorticity in Tropical Cyclone over the North Indian Ocean using WRF Model. Journal of Atmospheric Science Research. 6(3): 20-29. DOI: https://doi.org/10.30564/jasr.v6i3.5717

1. Introduction

A tropical cyclone maintains its life cycle by the energy that originates from the warmed moisture of the ocean surface. This warmed moisture releases latent heat in the eye wall of TC. The low-level inflow of moisture content wind and its spiraling upward motion flare up the PV of TC. The analysis of PV is a promising technique in meteorology. The facts from that analysis make the tropical cyclones (TC) more perceptible. Incorporating the concept of PV structure in current meteorology, forecasters and researchers may have many advantages in synoptic-scale forecasting of atmospheric events. Superposition of the upper PV anomaly and low-level centre nourish the TC's intensification [1].

The formation of a hollow tower of PV structure also favours the rapid intensification of TC. On the other hand, the detritions of PV structure decline the TC intensification [2,3]. Upper-level PV anomalies are crucial for storm motion. The impact of PV anomalies on the storm motions depends on the upper-tropospheric PV characteristics and corresponding locations of the vortex [4,5].

Upper-level PV streamer and middle-low-level PV anomalies exist in the genesis stage of the Mediterranean cyclone. Also, an acute PV tower stretches from the upper troposphere to the lower stratosphere found in one of the Mediterranean cyclones [6]. Convective heating gives rise to positive potential vorticity in and outside the ring area of TC. Positive potential vorticity at the matured stage of TC is crucial to maintaining the ring structure and the feedback process [7].

A narrow tower of maximum potential vorticity exists on the inner edge of the eyewall cloud of a matured Hurricane. In such a structure, potential vorticity can reach several hundred PV units [8]. Higher PV within the stratiform regions is the prime PV source for the intensification of TC [9]. Latent heat release originates the low-level PV. Vertical advection of latent heat broadens the low-level PV and stretches it up to the upper level [10,11].

The term annular heating function is suitable to describe the distribution of latent heat release in the eye wall of TC. Vertical advection of annular heating is more realistic than the descending of isentropes. The PV maximum exists adjacent to the radius of maximum heating [12]. The entropy difference between the air and sea allows more and more energy to TC from the underneath sea surface. The PV mixing from the eye wall to the inner core limits the entropy difference between the air-sea surfaces and prevents the TC intensity [13]. Heating the outer spiral rain bands declines the intensity of TC and increases the size of TC. Cooling the outer rain bands favour the strength and tightly packed inner core of TC [14].

Outward distribution of high PV from the inner core of TC raises the local isentropic surfaces and establishes a cold dome stretching from the mid to lower troposphere [15]. A considerable generation of PV in the rain band area is an indispensable factor for the secondary eyewalls in TC [16]. Concentric and compact eyewalls approaching smaller sizes exist in the intense stage of TC. Circular bands of maximum PV establish in the corresponding maximum vertical motions area of the eyewall and have powerful interaction with eyewall convection [17].

500 hPa level is considered half of the earth's troposphere. Below this level, the wind flow has the same direction. Hence atmospheric events at this level play a vital role in the genesis and intensification of TC. Fall of geopotential height cause turbulent weather phenomena. This atmospheric condition favour instability and convection of cloud accompanied by heavy rainfall [18]. The variation of geopotential heights of 500 hPa level may impact the dynamics of climate change via the change in circulation pattern [19].

The aim of this study is to find out the influence of upper PV on the dynamic parameters of TC over the NIO.

2. Synoptic study of TCs

A) **Ashoba:** A low-level cyclonic circulation developed over southeast AS on 5th June 2015 due to the southwest monsoon onset over Kerala. By the morning of 6th June, it moved northwards and concentrated into an LPA over the southeast and

adjoining east-central AS. Sufficient SST, low-level convergence, upper-level divergence, low-level relative vorticity and weak to moderate vertical wind shear favoured the concentration of the system into depression at 0300 UTC of 7th June over east-central AS. The system moved north-northwestward and intensified into DD at 0000 UTC on 8th June. At 0300 UTC on 8th June, the system turned into CS Ashoba. It continued its north-northwestward movement till 0900 UTC on 8th June and then moved northwards till 0600 UTC on 9th June. After that, it moved west-northwards till 0600 UTC on 10th June and west-southwestwards till 0000 UTC on 11th June. Later, the system moved westwards slowly and switched into DD at 1800 UTC on the 11th of June. It weakened into a depression at 0000 UTC on 12th June and WML over the northwest AS and adjoining Oman coast at 1200 UTC on 12th June.

B) **Titli:** A Very Severe Cyclonic Storm (VSCS) Titli formed over southeast BoB is considered in our present study. This system originated from the low-pressure area (LPA) over southeast BoB and adjoining north Andaman Sea at 0300 UTC on 7th October 2018. It intensified into a well-marked low (WML) at 1200 UTC on 7th October 2018. It then concentrated into a depression (D) over east-central BoB at 0300 UTC on 8th October 2018. The system advanced west north-westward and intensified into a deep depression (DD) over east central BoB at about 1800 UTC on 8th October 2018 and further intensified into cyclonic storm (CS) Titli at around 0600 UTC on 9th October 2018. It intensified into a severe cyclonic storm (SCS) at 2100 UTC on 9th October 2018 during its north-westward movement. Then it moved north-northwestwards at 0600 UTC on 10th October 2018 and evolved as a very severe cyclonic storm (VSCS), the highest intensification stage of its life cycle. It crossed north Andhra Pradesh and south Odisha coasts near Palasa at 18.8° N and 84.5° E during 2300 UTC on 10th October and 0000 UTC on 11th October 2018 as a VSCS. During this crossing, the wind speed was 140-150 Kmph gusting to 165 Kmph. It then moved north-westward and weakened into an SCS around 0600 UTC on 11th October and into a cyclonic storm (CS) around 1200 UTC of the same day. It turned into a DD over south Odisha at midnight (1800 UTC) on 11th October 2018.

C) **Mekunu:** A cyclonic circulation over Lakshadweep and its neighbourhood caused the formation of LPA over southeast AS at 0300 UTC on 20th May 2018. At 0000 UTC of 21st May, it appeared as a WML over the southwest and adjoining southeast AS. The Madden Julian Oscillation of phase 2 at 0300 UTC on 21st May favoured the cyclogenesis and further intensification. The environmental conditions such as SST, low-level relative vorticity, low-level relative convergence, upper-level divergence and vertical wind shear maintained the required value to sustain the cyclogenesis. This environmental condition continued till 1200 UTC on 21st May and the system concentrated as the depression over southwest and adjoining southeast AS. Weak to moderate vertical wind shear and successive increments of, low-level relative vorticity, low-level relative convergence, and upper-level divergence caused the further intensification of the system to DD at 0300 UTC on 22nd May. The system intensified as CS Mekunu at 1200 UTC on the 22nd, SCS at 0300 UTC, VSCS at 0900 UTC on the 23rd of May and reached its peak intensity ESCS at 0300 UTC on the 24th of May, 2018. It crossed the south Oman coast as ESCS between 1830 and 1930 UTC on 25th May 2018. By 0300 UTC on 27th May 2018, this system weakened into a WML over Saudi Arabia and adjoining areas of Oman & Yemen.

D) **Amphan:** A remnant of LPA over the south Andaman Sea and adjoining southeast BOB from 6th to 12th May 2020 influenced the formation of another fresh LPA over southeast BOB and adjacent south Andaman Sea at 0300 UTC on 13th May 2020. It became WML over southeast BOB and its neighbourhood at 0300 UTC on 14th May. Under favourable conditions, it turned into a depression (D) at 0000UTC and concentrated into DD at 0900UTC on 16th May over southeast BOB. After the north-northwestward movement, it developed as CS Amphan at 1200 UTC on 16th May 2020 over southeast BOB. It further intensified into a Severe Cyclonic Storm

(SCS) at 0300UTC, Very Severe Cyclonic Storm (VSCS) at 0900 UTC and Extremely Severe Cyclonic Storm (ESCS) at 2100 UTC on 17th May. At 0600 UTC on 18th May 2020, it intensified into Supper Cyclonic Storm (SuCS). This stage lasted about 24 hours and weakened into ESCS over west-central BOB at 0600 UTC on 19th May. It crossed the West Bengal-Bangladesh coasts as a VSCS across Sundarbans during 1000-1200 UTC on 20th May with a maximum sustained wind speed of 155-165 Kmph.

3. Data and methods

The WRF model version 4.0.3 is used to simulate the dynamic features of TCs. The model runs took place following the best track position and status provided by the satellite observations of the Indian Meteorological Department (IMD) (**Table 1**). We used NCEP FNL reanalysis 1 × 1 degree data in the simulations. A one-way nesting method is used to set up the domains. The horizontal resolutions of parent and child domains were 21 and 7 km. Arakawa C-grid staggering was used as grid distribution. Mercator map used in projection for the model run. A coupling of the Kain-Fritsch (new Eta) scheme and WSM6-class graupel scheme as cumulus and microphysics option was used in the runs. Ertel's hydrostatic potential vorticity equation $PV = -g(\zeta_\Theta + f)\frac{\partial \Theta}{\partial p}$ used in this study, where ζ_Θ is the relative vorticity, f is the coriolis parameter, g is the gravitational acceleration, Θ is the potential temperature and p is the pressure. This study was accomplished using the outputs of the inner domain of 10° × 10° **areal extent**. We calculated maximum PV at 200 hPa level, wind speed at 850 hPa, central pressure and vertical wind shear between 850 and 200 hPa within the corresponding area of the inner domain. We also calculated the geopotential height GPH = $\frac{\Phi}{g_0}$, where $\Phi = gz$ the geopotential and g_0 is the standard value of gravitational acceleration. We visualized the model outputs using the GrADS software. The model outputs compared with the ECMWF Reanalysis 5th Generation (ERA5) hourly data of 0.25° × 0.25° horizontal resolution.

4. Results and discussion

4.1 Temporal evolution of upper potential vorticity

The analysis of PV for forecasting the genesis and intensification of TC is very significant in current meteorology. The temporal evolution of upper tropospheric PV may give us important insights into the intensification of TC. Therefore, the facts and findings from the PV analysis will enrich the present forecasting system. At least 1 PVU is required to sustain the TC intensification shown in the PV's time evolution for the matured TCs. The time evolution of PV in the model and ECMWF is comparable (**Figure 1**). For Amphan and Mekunu, the model and ECMWF have calculated PVs that are close to each

Table 1. Schedule of WRF model run following IMD satellite-based best track positions.

Event Name	Location	Model run start at	Model run end at	Initial condition	End condition	Maximum intensity during model run
Ashoba	AS	0600UTC of June 08, 2015	0600UTC of June 11, 2015	CS	CS	CS
Titli	BOB	0600UTC of October 09, 2018	0600UTC of October 12, 2018	CS	DD	VSCS
Mekunu	AS	1200UTC of May 22, 2018	1200UTC of May 25, 2018	CS	ESCS	ESCS
Amphan	BOB	1200UTC of May 16, 2020	1200UTC of May 19, 2020	CS	ESCS	SuCS

*DD: Deep Depression, CS: Cyclonic Storm, VSCS: Very Severe Cyclonic Storm, ESCS: Extremely Severe Cyclonic Storm, SuCS: Supper Cyclonic Storm.

other most of the time. The ups and downs of upper PVs have a similar fashion in all TCs. In the peaks of upper PV from the model, the TCs experienced the maximum intensity. A significant contribution to PV comes from the term where is the potential temperature and p is the pressure. Hence model and ECMWF calculated comparatively higher PV in TCs over the BOB because of the warmer than AS. The model used NCEP FNL reanalysis of six hourly 1 × 1 degree data as input. The results compared with the corresponding values come from the globally scaled ECMWF reanalysis high-resolution 5th Generation (ERA5) hourly data of 0.25° × 0.25°. Therefore, the results from the model may differ slightly from the corresponding values of ECMWF. Hence the results from the model outputs have shown that the WRF model successfully simulated the parameters used to calculate PV.

4.2 Intensification of TC

There are many challenges in the intensity forecasting of TC due to the lack of observations. Therefore to improve the existing forecasting system, meteorologists have been taking numerous measures. The use of the PV technique in the analysis of TC intensity may yield new insights into the NIO. Low pressure at the centre and wind speed around the centre are important parameters to measure the intensity of TC.

Central pressure

The central pressure calculated by the model appeared as though upper PV suppressed the central pressure of the TCs. The increase of the upper tropospheric PV caused a decrease in the central pressure. Such inverse relation was maintained in all the studied events for a particular time (**Figure 2**). This inverse relation continued until the upper PV reached below 3×10^{-6} $m^2s^{-1}KKg^{-1}$. Pressure drop continued in Mekunu over the whole period of model run (**Figure 2**). In Amphan, the pressure drop stopped over the last 24-hour spell even though it had sufficient upper PV and underwent decay. Such behaviour of upper PV in Amphan requires extensive study.

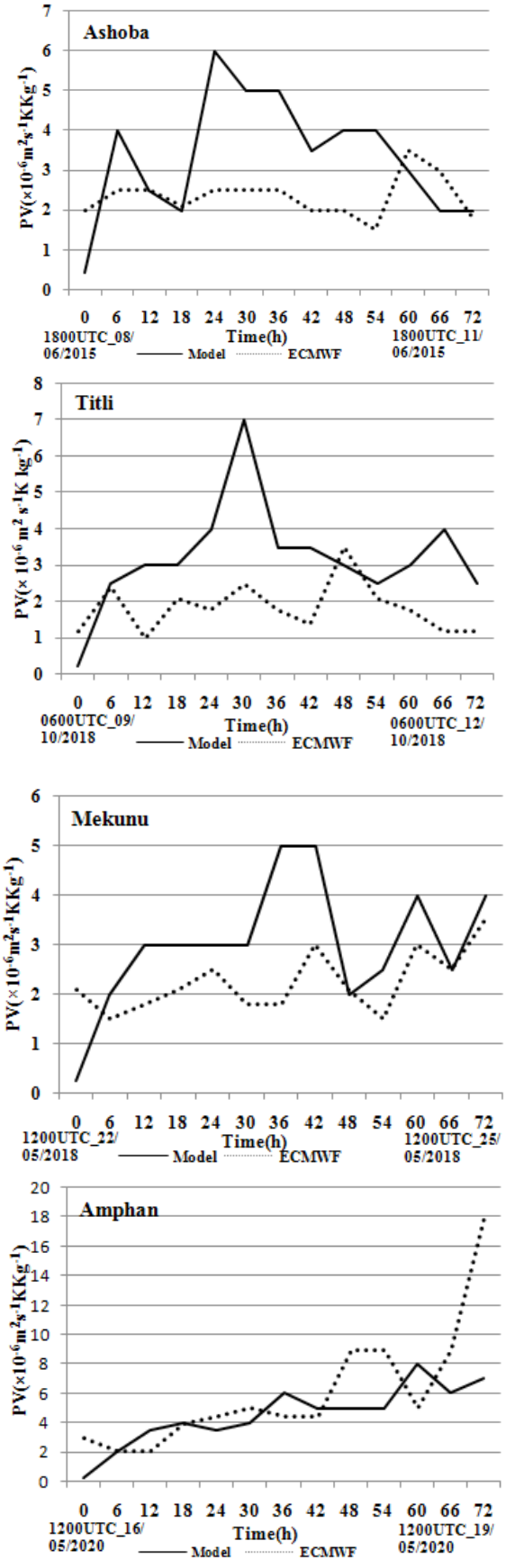

Figure 1. Time evolution of 200 hPa level PV.

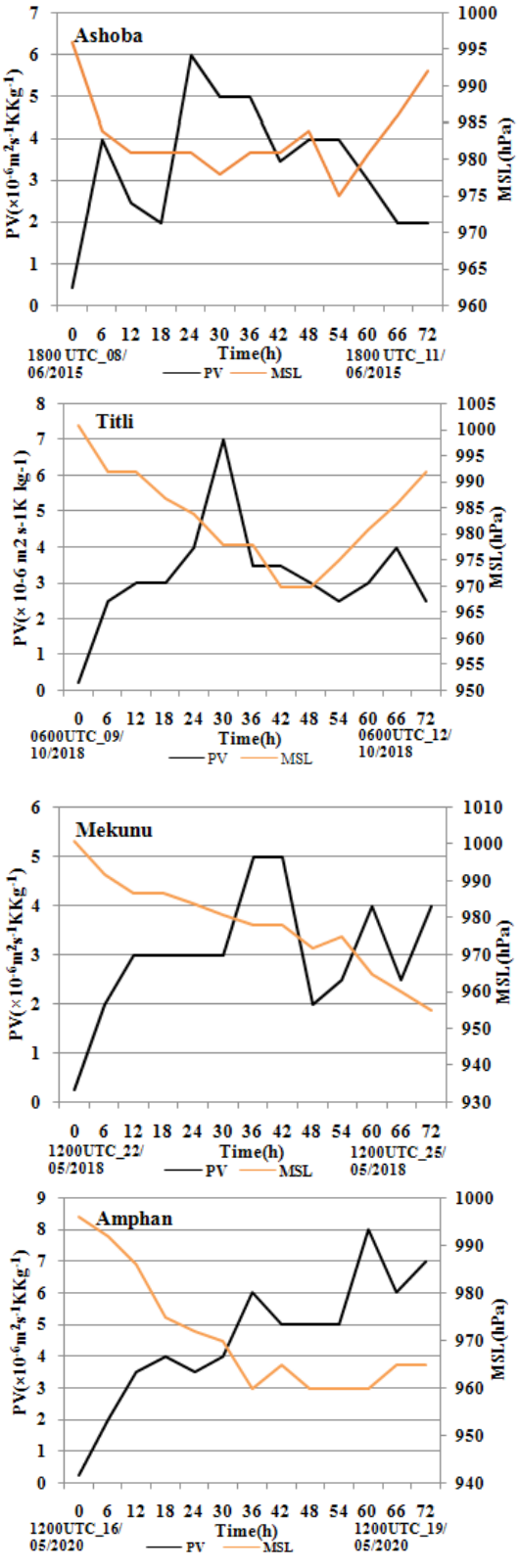

Figure 2. Variation of the model calculated 200 hPa level PV with central pressure.

Wind

Dry and warm conditions are the dominant features of the centre of TC. The most devastating and threatening phenomena exhibited by the eyewall of TC. The interaction between upper PV and low-level wind speed is significant in the eye wall region. The low-level maximum wind speed computed by the model was found closer to that of ECMWF values. The peak values of low-level wind by the model followed the corresponding peak values of ECMWF (**Figure 3**). Comparatively, ECMWF computed wind speeds are of smaller values. The low-level wind speed was found incremental with upper PV over the ocean surface in all the studied events. Almost all of the cyclones we studied found high wind speeds at the peak of the upper PVs (**Figure 4**). Therefore, higher PV favoured the intensification of TCs.

4.3 PV and shear

Wind shear removes the energy in terms of heat and moisture from the TC core. Wind shear causes the TC vortex to tilt away from its base. The high wind shear resists the formation and intensification of TC. Therefore, wind shear is a significant parameter for the genesis and intensification of TC. The wind shear and upper PV exhibited almost identical temporal evolution. The PV line has appeared as though simultaneously it works as a suppressor and exaggerator of the wind shear. That is, it seems as if the upper PV acts as a regulator of the wind shear. In Mekunu, the wind shear didn't exceed the threshold value (12 ms^{-1}) required for the formation and intensification of TC for the whole period of the model run. In Ashoba, Titli and Amphan, the wind shear during the last 12 hours spell of the model run was found negative and above the threshold value. Such characteristics of the wind shear forced the decay of Ashoba, Titli and Amphan though they had sufficient upper PV (**Figure 5**). This relationship between upper PV and wind shear requires further extensive study for accurate forecasting.

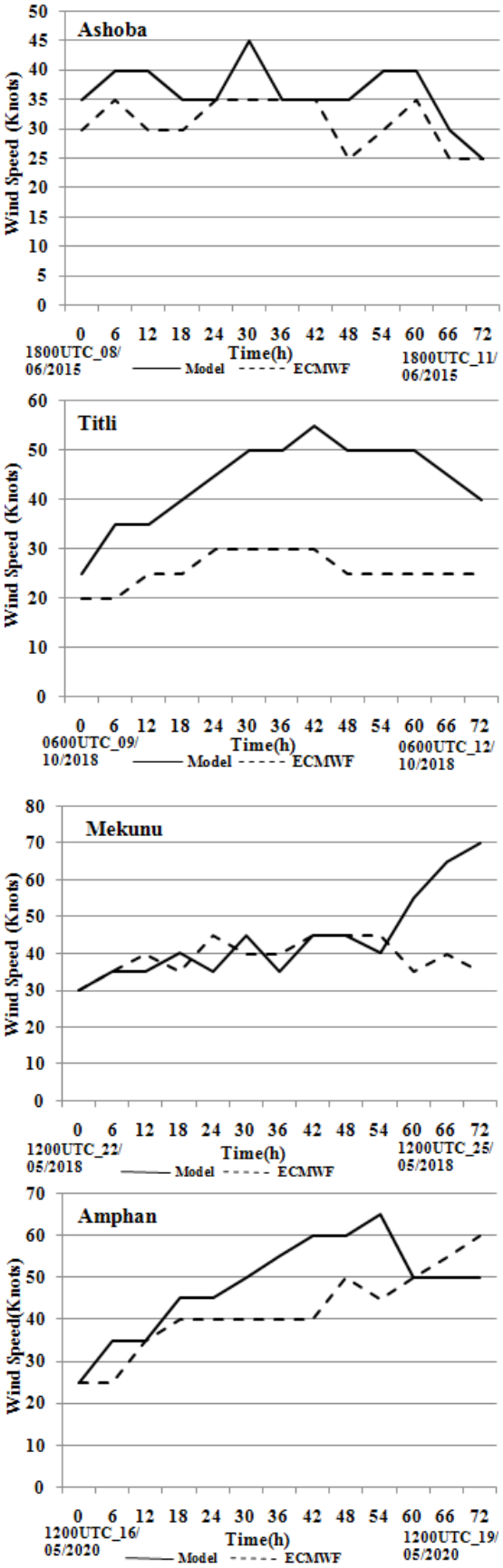

Figure 3. Variation of 850 hPa wind speed with time by model and ECMWF.

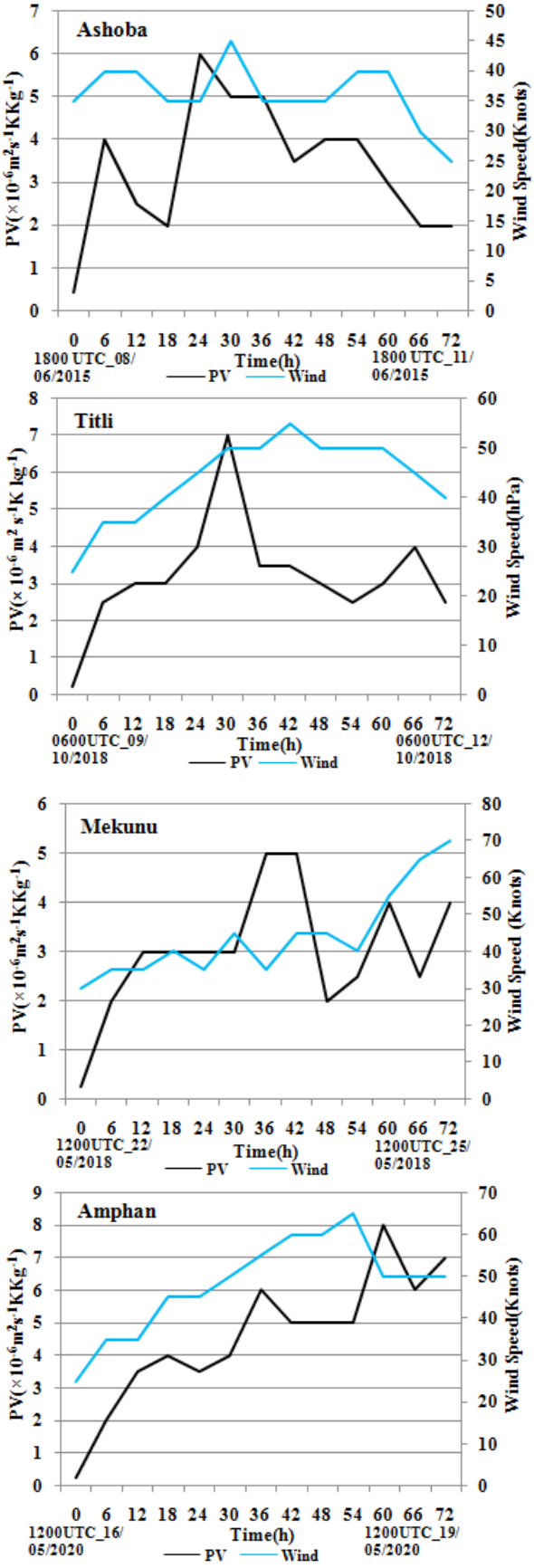

Figure 4. Evolution of 200 hPa level PV and 850 hPa maximum wind speed.

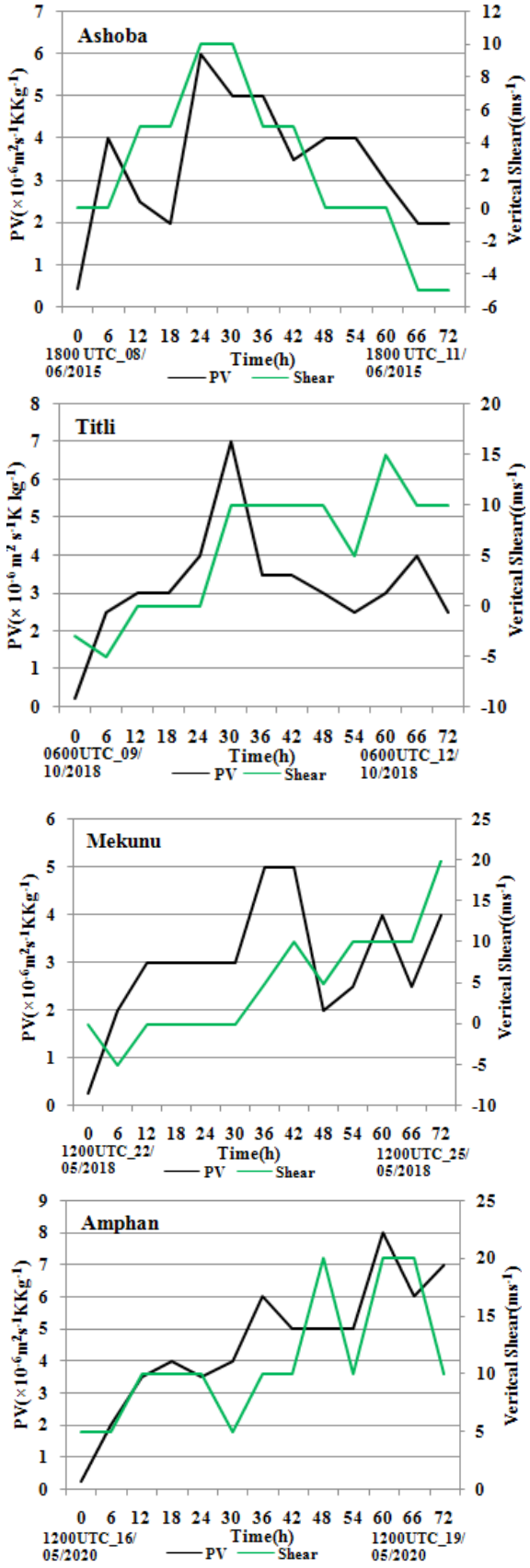

Figure 5. Variation of 200 hPa PV and vertical wind shear with time by model.

4.4 Geopotential height of 500 hPa level

The 500 hPa level in the troposphere has considerable importance for forecasting storms. The wind flow below this level is almost in the same direction. As a result, any event occurring at this level substantially affects the weather below it. Variations in geopotential height at the 500 hPa level affect various atmospheric events at the sea surface. High and low geopotential heights at the said level produce ridges and troughs. Anti-cyclones and cyclones form gradually under these ridges and troughs at sea level. The geopotential heights decrease with the increase of upper PV. The model results show that the upper PV and geopotential heights alternate mutually in opposite trends over the ocean. Acute fall of geopotential height found in Titli, Mekunu and Amphan with the rising of upper PV. Ashoba experienced a slower decline in geopotential height and didn't favour the intensification. The lowering of geopotential height continued over the whole period of the model run of Mekunu and kept up its intensification. A sharp fall of geopotential height found in Titli, Mekunu and Amphan underwent decrying (**Figures 4 and 6**).

5. Concluding remarks

Previous research has shown that upper PV dominates the genesis and intensification of TC. Studies have also shown that upper PV plays a significant role in steering TC's motion. As PV has an implicit effect on tropical cyclone intensification, there is a need for research on the relationship of dynamical parameters with upper PV in the NIO. Fine-scale observational study of PV structure may provide unrevealed insights into TC intensifications. To unearth the role of PV in the structure and intensity change of TC over the NIO is crucial. The following insights are the outcomes of the present study:

1) At least 1 PVU upper PV is required to maintain the intensification of TC.

2) In BOB, upper PV was found higher than that of AS.

3) An increase in upper PV accelerates the pressure drop in the centre of the TC.

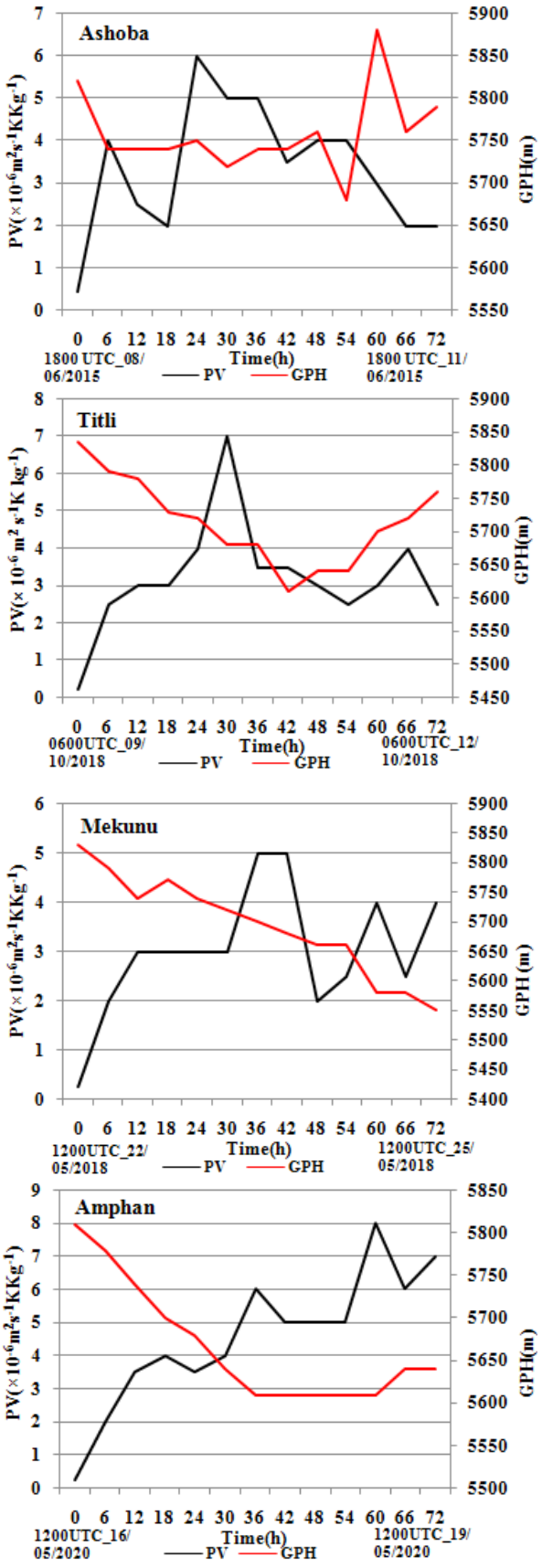

Figure 6. Temporal variation of 200 hPa level PV and 500 hPa level geopotential height in the model.

4) The rise in upper PV favours the low-level wind speed over the ocean.

5) The wind shear and upper PV exhibit almost similar temporal evolution over the ocean.

6) The TCs with negative wind shear and wind shear above the threshold value of 12 m/s couldn't intensify even if they had sufficient upper PV.

7) The upper PV and geopotential heights change in opposite trends.

The results obtained from the present study will play a significant role in forecasting tropical cyclones in the Bay of Bengal basin. Furthermore, considerable attention should pay to the effect of upper PV on atmospheric dynamic and thermodynamic instability.

Author Contributions

A.H.M. Fazla Rabbi (Corresponding author) engaged with the model run, record keeping, data analysis, interpretation and drafting of the manuscripts. Ishtiaque M. Syed and Md. Abdullah Elias Akhter (Co-authors) was involved with designing, providing suggestions and editing the manuscript. M A K Mallik (Co-author) was concerned with reasoning, planning and computing.

Conflict of Interest

There is no conflict of interest among the authors as well as the funder.

Funding

University Grants Commission of Bangladesh financed the research to carry on.

Acknowledgement

The authors acknowledge the financial support from the University Grants Commission of Bangladesh. We express our deep gratitude to the Bangladesh Meteorological Department for giving us extensive technical assistance. We thank National Centres for Environmental Prediction (NCEP) and European Centre for Medium-Range Weather Forecasts(ECMWF) for providing reanalysis data to us.

References

[1] Molinari, J., Skubis, S., Vollaro, D., et al., 1998. Potential vorticity analysis of tropical cyclone intensification. Journal of the Atmospheric Sciences. 55(16), 2632-2644.

[2] Martinez, J., Bell, M.M., Rogers, R.F., et al., 2019. Axisymmetric potential vorticity evolution of Hurricane Patricia (2015). Journal of the Atmospheric Sciences. 76(7), 2043-2063. DOI: https://doi.org/10.1175/JAS-D-18-0373.1

[3] Schubert, W.H., Slocum, C.J., Taft, R.K., 2016. Forced, balanced model of tropical cyclone intensification. Journal of the Meteorological Society of Japan. 94(2), 119-135. DOI: https://doi.org/10.2151/jmsj.2016-007

[4] Wu, C.C., Emanuel, K.A., 1995. Potential vorticity diagnostics of hurricane movement. Part II: Tropical storm Ana (1991) and Hurricane Andrew (1992). Monthly Weather Review. 123(1), 93-109.

[5] Schubert, W.H., Montgomery, M.T., Taft, R.K., et al., 1999. Polygonal eyewalls, asymmetric eye contraction, and potential vorticity mixing in hurricanes. Journal of the Atmospheric Sciences. 56(9), 1197-1223.

[6] Miglietta, M.M., Cerrai, D., Laviola, S., et al., 2017. Potential vorticity patterns in Mediterranean "hurricanes". Geophysical Research Letters. 44(5), 2537-2545. DOI: https://doi.org/10.1002/2017GL072670

[7] Wu, C.C., Wu, S.N., Wei, H.H., et al., 2016. The role of convective heating in tropical cyclone eyewall ring evolution. Journal of the Atmospheric Sciences. 73(1), 319-330. DOI: https://doi.org/10.1175/JAS-D-15-0085.1

[8] Hausman, S.A., Ooyama, K.V., Schubert, W.H., 2006. Potential vorticity structure of simulated hurricanes. Journal of the Atmospheric Sciences. 63(1), 87-108.

[9] May, P.T., Holland, G.J., 1999. The role of potential vorticity generation in tropical cyclone rainbands. Journal of the Atmospheric Sciences. 56(9), 1224-1228.

[10] Schubert, W.H., Alworth, B.T., 1987. Evolution of potential vorticity in tropical cyclones. Quarterly Journal of the Royal Meteorological Society. 113(475), 147-162.

[11] Rozoff, C.M., Kossin, J.P., Schubert, W.H., et al., 2009. Internal control of hurricane intensity variability: The dual nature of potential vorticity mixing. Journal of the Atmospheric Sciences. 66(1), 133-147. DOI: https://doi.org/10.1175/2008JAS2717.1

[12] Möller, J.D., Smith, R.K., 1994. The development of potential vorticity in a hurricane-like vortex. Quarterly Journal of the Royal Meteorological Society. 120(519), 1255-1265.

[13] Yang, B., Wang, Y., Wang, B., 2006. The effect of internally generated inner-core asymmetries on tropical cyclone potential intensity. Journal of the Atmospheric Sciences. 64(4), 1165-1188. DOI: https://doi.org/10.1175/JAS3971.1

[14] Wang, Y., 2008. How do outer spiral rainbands affect tropical cyclone structure and intensity? Journal of the Atmospheric Sciences. 66(5), 1250-1273. DOI: https://doi.org/10.1175/2008JAS2737.1

[15] Deng, D., Davidson, N.E., Hu, L., et al., 2017. Potential vorticity perspective of vortex structure changes of tropical cyclone Bilis (2006) during a heavy rain event following landfall. Monthly Weather Review. 145(5), 1875-1895. DOI: https://doi.org/10.1175/MWR-D-16-0276.1

[16] Judt, F., Chen, S.S., 2010. Convectively generated potential vorticity in rainbands and formation of the secondary eyewall in hurricane Rita of 2005. Journal of the Atmospheric Sciences. 67(11), 3581-3599. DOI: https://doi.org/10.1175/2010JAS3471.1

[17] Yau, M.K., Liu, Y., Zhang, D.L., et al., 2004. A multiscale numerical study of hurricane Andrew (1992). Part VI: Small-scale inner-core structures and wind streaks. Monthly Weather Review. 132(6), 1410-1433.

[18] Jabbar, M.A.R., Hassan, A.S., 2022. Evaluation of geopotential height at 500 hPa with rainfall events: A case study of Iraq. Al-Mustansiriyah Journal of Science. 33(4), 1-8. DOI: http://doi.org/10.23851/mjs.v33i4.1161

[19] Christidis, N., Stott, P.A., 2015. Changes in the geopotential height at 500 hPa under the influence of external climatic forcings. Geophysical Research Letters. 42(24), 10798-10806. DOI: https://doi.org/10.1002/2015GL066669

BILINGUAL PUBLISHING GROUP

Journal of Atmospheric Science Research

https://journals.bilpubgroup.com/index.php/jasr

ARTICLE

Relationship and Variability of Atmospheric Precipitation Characteristics in the North-West of Ukraine

Svetlana Vasilievna Budnik

The Central Geophysical Observatory of a Name of Boris Sreznevsky, Kyiv, 02000, Ukraine

ABSTRACT

The paper deals with the issues of differentiation of atmospheric precipitation into gradations according to their characteristics and established meteorological practices. The division of atmospheric precipitation into gradations allows one to have an idea of the possible consequences of their fallout on life in the area. The dependence of the average intensity of precipitation on their duration for the entire series of observations is not described by a power-law dependence with a sufficient degree of reliability, and when differentiating into gradations according to the amount of precipitation (< 2.5 mm, 2.5-10 mm, ≥ 10 mm), the dependences are obtained with a high degree of correlation. The scatter of points can be explained by the presence of intermediate categories of precipitation, which does not take into account the accepted division of the data. Thus, for large values of the amount of precipitation, the existence of a separate curve is possible, since the existing classifications of precipitation imply the division of heavy showers into separate gradations. Differentiation of rains by their duration shows a stronger stratification of the field of points for shorter rains (up to 60 minutes). This stratification of the field of points is successfully differentiated into shorter segments of 20, 30 minutes. Associated with the greater heterogeneity of shorter precipitation, it can be both rains of low intensity and heavy downpours of short duration. The probability of the position of the maximum intensity of precipitation during rain has more significant differences for precipitation less than 2.5 mm (the curves are more curved). For rains with a precipitation amount of 2.5 mm or more, the probability curves approach straight lines, which is associated with greater heterogeneity of precipitation less than 2.5 mm.

Keywords: Precipitation; Gradation; Intensity; Duration; Shower

*CORRESPONDING AUTHOR:

Svetlana Vasilievna Budnik, The Central Geophysical Observatory of a Name of Boris Sreznevsky, Kyiv, 02000, Ukraine; Email: svetlana_budnik@ukr.net

ARTICLE INFO

Received: 17 April 2023 | Revised: 18 July 2023 | Accepted: 31 July 2023 | Published Online: 5 August 2023

DOI: https://doi.org/10.30564/jasr.v6i3.5657

CITATION

Budnik, S.V., 2023. Relationship and Variability of Atmospheric Precipitation Characteristics in the North-West of Ukraine. Journal of Atmospheric Science Research. 6(3): 30-40. DOI: https://doi.org/10.30564/jasr.v6i3.5657

1. Introduction

Atmospheric precipitation is an integral part of the cycle of substances in nature. They carry out the moistening of the territory, dissolution and transportation of substances on the surface of the earth and in the soil layer, which contributes to the interaction of all elements in natural and territorial complexes, which, in turn, ensures the development of vegetation, the existence of animals and humans as well.

Various manifestations of atmospheric precipitation (dew, hail, drizzle, rains, showers, etc.) are important for ecosystems. Humidification of the territory is provided not only by showers, but also by smaller rains, especially in areas where their percentage of the total precipitation is the largest.

Actually, low-intensity rains provide replenishment of groundwater reserves and support low-water runoff in rivers, have a beneficial effect on the development of vegetation cover and, as a result, reduce the heating of the soil surface and evaporation. Downpours are responsible for floods and soil erosion, which often leads to large material costs, however, in the current physical and geographical conditions, they also provide channel formation and ecological cleaning of river channels.

The question arises of dividing atmospheric fallout (precipitation) into gradations that allow one to have an idea of their possible influences on natural and economic processes and human life in a given area.

Precipitation is divided by origin and by the nature of precipitation, they are divided into types, views, and classes. There are types of precipitation: cyclonic, convective and orographic. Types of precipitation: drizzle, rain, ice, freezing rain, snow, snow pellets, ice pellets, and hail [1,2].

As criteria for dividing atmospheric precipitation into gradations, such consequences of rainfall as the beginning of runoff formation, erosion of the soil surface, the formation of mudflows, etc. are also used.

There is no generally accepted division of genetically different types of sediments according to morphometric features [3,4]. The most common morphological definitions relate to shower and non-storm precipitation and are conditional. The reason for this may be the physical and geographical features of the area under study [5]. Showers are typical for arid regions and, in particular, for the forest-steppe and steppe zones of the European territory of the USSR [2] and are characterized by great diversity and local distribution, covering at the same time, as a rule, small areas of the order of tens, less often hundreds of square kilometers.

The first researcher of showers in Russia, E.Yu. Berg, considered showers as the most intense areas of rain with an average intensity of more than 0.5 mm/min with a duration of 5 minutes, etc. [2,5,6].

A.I. Voeikov proposed to consider rain with an intensity of at least 0.5 mm/min as a downpour [7]. In other countries, the shower is determined by different intensity figures [7]: Switzerland (Riggenbach)—0.34, America (Fassig)—1.28 mm/min, England (Simon)—0.76 mm/min, Germany (Gellmann)—1.01 mm/min.

As mentioned, there are differences in the definition of showers among states—for example, in Canada it is considered light rain at 0.2 mm/h and heavy rain at 7.6 mm/h [8].

Currently, rains with an intensity of up to 2.5 mm/h (0.04 mm/min) are often considered light rain, rains with a precipitation intensity of 2.5-7.5 mm/h (0.04-0.125 mm/min). Heavy rains are considered with an intensity of more than 7.5 mm/h (more than 0.125 mm/min).

Drizzle is considered light drizzle < 0.1 mm/h, moderate drizzle 0.1-0.5 mm/h, heavy drizzle 0.5 mm/min [9]. The rain is classified as light rain < 2.5 mm/h, moderate rain 2.5 to 10.0 mm/h, and heavy rain over 10.0 m/h. Rainfall over 50 mm/h is considered heavy.

In Spain [4], the National Meteorological Institute has defined the following average hourly intensity (I) thresholds: light rainfall $I \leq 2$ mm/h, moderate rainfall $2 < I \leq 15$ mm/h, heavy rainfall $15 < I \leq 30$ mm/h, very heavy rainfall $30 < I \leq 60$ mm/h, heavy rain $I > 60$ mm/h. However, these thresholds vary

considerably from one country to another, which means that it would be difficult to obtain a universal classification based on different thresholds [4].

Rains with a precipitation amount of up to 10 mm are considered light, 11-30 mm—moderate, 31-50—heavy, and more than 51 mm—very heavy [10].

In the territory of Ukraine, the intensity of precipitation increases from north to south [11]. The highest maximum intensity for a 5-minute interval in the southern steppe zone (including the steppe part of the Crimea) and Transcarpathia reach 30-40 mm/min, in the northern part of Ukraine—20-30 mm/min. The highest maximum precipitation intensity for a 10-minute interval is much lower than for a 5-minute interval, and reaches 2.5-3 mm/min in the southern steppe, the steppe part of the Crimea and Transcarpathia, and 1.0-2 in the northern part of the territory 2 mm/min.

Studies of the seasonal dynamics of large-scale and convective precipitation in the territory covering the East European Plain and the Black Sea region revealed an excess (2 times) of the number of showers over precipitation [12].

Our study of rains with more than 10 mm of precipitation in the Northwest of Ukraine showed that at the present stage of climate change in the Northwest of Ukraine, there is a general tendency to increase the amount of precipitation per year. This trend is not the same across the territory and depends on the height and latitude of the area. The amount of precipitation varies both in space and time, but the distribution of the characteristics of the rains themselves (intensity, duration, and others) continues to be similar throughout the researched territory [13,14].

The creation of automated precipitation tracking systems (radar complexes, etc.) in recent years requires the same autonomous system for their differentiation and recognition [10]. Deepening and refining our understanding of the structure and relationships in rainfall will make it possible to make the right decisions in their forecasting. Making decisions based on the results of observations and forecasts also requires specification in terms of precipitation gradations in order to prevent damage to the economy of the region and the population.

The task of this work was to identify the features of grouping the range of changes in rain characteristics with different parameters. To trace the relationship and change in the characteristics of rains (their number, intensity, duration) of different gradations over time in the Northwest of Ukraine.

2. Materials and methods of research

The analysis used materials from observations of all rains that could be recorded at meteorological stations in Kyiv and Kamenka-Bugskaya. The locations of the stations on the territory of Ukraine were presented earlier [14] (**Figure 1**).

The completeness and coverage of the range of precipitation measured at meteorological stations are presented in **Tables 1-2**. The order and trend of changes in the characteristics of rain for the two weather stations, in general, coincide.

Table 1. Characteristics of the series of observations of atmospheric precipitation at meteorological stations Kyiv and Kamenka-Bugskaya.

Characteristics	**Weather stations**	
	Kyiv	Kamenka-Bugskaya
Precipitation observation period, total (number of years of observation)	1856-2020 (162)	1894-1905, 1932-1934, 1946-2020 (89)
Period of observations with pluviographs, total (number of years of observations)	1913, 1924-1929, 1950-1980, 1993-2020 (59)	1963-1985-1988-2018 (56)
Average long-term precipitation per year, mm	599	645
Range of changes in the amount of precipitation per year, mm	331-925	311-959

Table 2. Characteristics of rainfall observation series for meteorological stations Kyiv and Kamenka-Bugskaya.

Weather station	Characteristics	Precipitation, mm			
		less than 2.5 mm (by 1970)	2.5-10 mm	10 mm or more	All
Kyiv	number of recorded rains	738	1112	407	2257
	Precipitation range for rain, mm	0.1-2.4	2.5-9.9	10-76.7	0.1-76.7
	Range of average intensity of precipitation for rain, mm/min	0.00085-0.58	0.002-1.2	0.01-0.60	0.00085-1.2
	Range of maximum intensity of precipitation for rain, mm/min	0.00097-0.8	0.002-3.15	0.013-7.1	0.00097-0.71
	Precipitation duration range for rain, min	1-567	6-1837	21-2218	1-2218
Kamenka-Bugskaya	number of recorded rains	85	1355	521	1961
	Precipitation range for rain, mm	0.4-2.4	2.5-10	10-98.5	0.4-98.5
	Range of average intensity of precipitation for rain, mm/min	0.01-0.22	0.01-1.02	0.01-1.58	0.01-1.58
	Range of maximum intensity of precipitation for rain, mm/min	0.02-0.53	0.01-3.0	0.03-2.62	0.01-3.0
	Precipitation duration range for rain, min	3-423	5-1272	11-2505	3-2505

On the network of the hydrometeorological service of Ukraine, observations of heavy rains have been introduced since 1934-1935 [15], however, observations of the course of atmospheric precipitation, including rainfall, with the help of pluviographs at individual weather stations were also carried out earlier (from the end of the 19th to the beginning of the 20th century). Since 1961, dew has been excluded from the number of observed phenomena, only its presence is noted without describing the time of the beginning and end of the phenomenon and its intensity, which was noted according to the instructions for meteorological stations in 1928-1935 [16]. Instructions to weather stations in 1954 and 1958 [17,18] emphasize that heavy rain determines the nature of rainfall, and not the amount of precipitation, which may be insignificant. Heavy rain has a significant intensity of precipitation in a short time. The amount of precipitation here may be less than that of rains with low intensity but long duration.

Rain observations with the help of a pluviograph at the studied meteorological stations were carried out with interruptions in observations for almost 100 years at the Kyiv meteorological station and 56 years at the Kamenka-Bugskaya meteorological station. Rain records were made using a Gelman pluviograph with a receiving area of 500 cm^2. During this time, the approach to the analysis of recorder tapes (pluviographs) and the selection of pluviograph records for analysis changed. Unfortunately, materials deciphering the tapes of the pluviograph until 1952 according to the Kyiv weather station have not been preserved.

So, until 1935 [19], heavy rains were selected for analysis and publication according to the E. Berg norms (**Table 3**) [6], where showers were understood as rains during which, for a given time, the rain intensity did not fall below values presented in **Table 3**. Later [4], the processing of tapes was carried out according to the method presented in the Manual for Hydrometeorological Stations and Posts [18], in the collection [15] materials were published on rains,

the amount of precipitation for which was 10 mm or more. Priority in the publication of data on observations of the course of rains using pluviographs with a rainfall of 10 mm or more has been preserved to this day [20].

Table 3. The norms of E.Yu. Berg (1905) in the definition of the concept of shower [6].

Shower duration, min	The amount of precipitation for the specified time, mm	Shower intensity, mm/min
5	2.5	0.50
10	3.8	0.38
15	5.0	0.33
20	6.0	0.30
25	7.0	0.28
30	8.0	0.27
35	9.0	0.26
40	9.6	0.24
45	10.25	0.23
50	11.00	0.22
10	12.00	0.20
120	18.00	0.15
240	27.00	0.11
720	45.00	0.06
1440	60.00	0.04

Until the 1970s, data on decoding tapes of pluviographs with all recorded liquid atmospheric precipitation were placed in TM-14; later, only materials with precipitation of 2.5 mm or more began to be placed there. Since 1984, the data of observations with the help of pluviographs for rains with a precipitation amount of 2.5 mm or more have been placed in the TMS-1 summary meteorological tables. In addition, at most meteorological stations, rainfall is recorded with the help of pluviographs from May to September (this also applies to the Kamenka-Bugskaya meteorological station).

However, for individual weather stations, including the Kyiv weather station, in recent years, rain observations with the help of pluviographs were carried out from 2009 to 2013 from April to November, and since 2014 they have been carried out almost monthly (if weather conditions permit). That is, the series of observations of precipitation are not homogeneous according to several criteria—the time of observation and the boundary conditions of selection (2.5 mm or more).

However, if we also take into account the periods when the pluviographs were not able to record the falling precipitation (the intensity and amount of precipitation exceeded the limits of the speed of the device or the breakdown of the device mechanisms, etc.), then there will be even more heterogeneous breaks in the rows. However, in general, the series under consideration can be considered assets of random variables characterizing the corresponding periods.

In the study of the presented materials, a graphical-analytical method, descriptive statistics, elements of probability theory and regression analysis were used.

3. Results

Many researchers [2,5,7,21,22] confirm the existence of a close relationship between the duration of showers and their average intensity. The highest mean intensities occur during short showers. The longer the duration of the shower, the lower its average and maximum intensity. Most researchers believe that these dependencies are characterized by a power function [6].

Studies show that the dependence of the amount of precipitation on their duration is positive, but the field of points is strongly dispersed from year to year. The grouping of years according to the amount of atmospheric precipitation per year brings the communication lines somewhat closer, but the dispersion of points remains.

The existing practice of processing rain observation data using pluviographs [15], used in the USSR and Ukraine, including (as mentioned above), makes it possible to distinguish between the available series of rain observations into three gradations: 1) less than 2.5 mm, 2) 2.5-10.0 mm, 3) more than and equal to 10 mm, and analyze the presence of differences between these gradations.

Thus, the dependence of the average intensity of precipitation on their duration for the entire series is not described by a power-law dependence with a suf-

ficient degree of reliability, and when differentiated into these gradations, the dependences are obtained with a high degree of correlation (**Figures 1 and 3**).

The scatter of points can be explained by the presence of intermediate categories, which does not take into account the accepted division of the data. Thus, for large amounts of precipitation, the existence of a separate curve is possible, since the existing classifications of precipitation imply the division of heavy showers into separate gradations (heavy, mountainous, Texas, etc.) [23]. **Figure 2** clearly confirms this.

Rains of varying intensity and duration affect the water balance of the study area and the economic indicators of the region's development stability in different ways. The probability of precipitation with different intensity and duration is shown in **Figures 4-6**. According to the classifications of precipitation discussed above, the probability of occurrence of rains of different "power" of impact on natural and economic systems is different (**Table 4**).

The experience of meteorological and climatic studies [3] shows that a fairly reliable and clear criterion for separating precipitation, reflecting both genetic and morphometric features, is their duration. All rains according to this criterion [3] are divided into rains lasting < 1 h, from 1 to 3 h and more than 3 h. So, on a meteorological station Kyiv Kamenka-Bugskaya (**Figures 7 and 9**) the differentiation of rains on their duration shows stronger stratification of a field of points for less long rains (till 60 minutes). This stratification of the field of points successfully differentiates into shorter time intervals (**Figure 8**) of 20, 30 minutes.

The general field of points is strongly scattered. However, when data are differentiated by precipitation duration, this chaos of points becomes more ordered. The deepening of differentiation by the duration of precipitation of shorter rains increases the tightness of the grouping of points near the trend lines. Different colors show the dependence of the intensity of precipitation on their amount for different durations.

According to a number of authors [3], the course

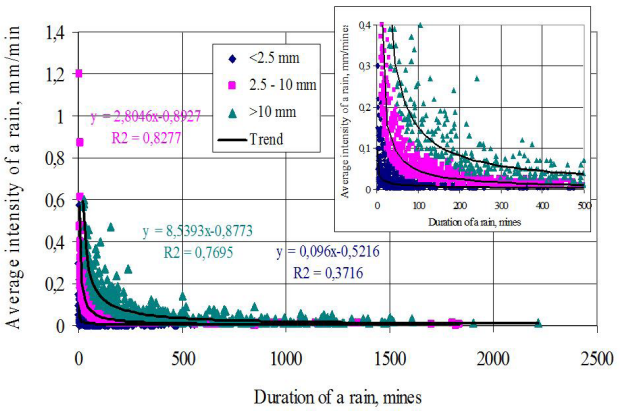

Figure 1. The dependence of the average intensity of precipitation on their duration at the Kyiv weather station, differentiated by the amount of precipitation per rain.

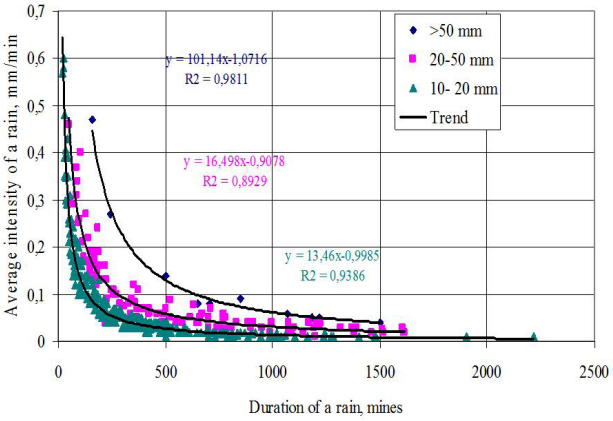

Figure 2. Dependence of the average intensity of precipitation over 10 mm on their duration according to the Kyiv meteorological station, differentiated by the amount of precipitation per rain.

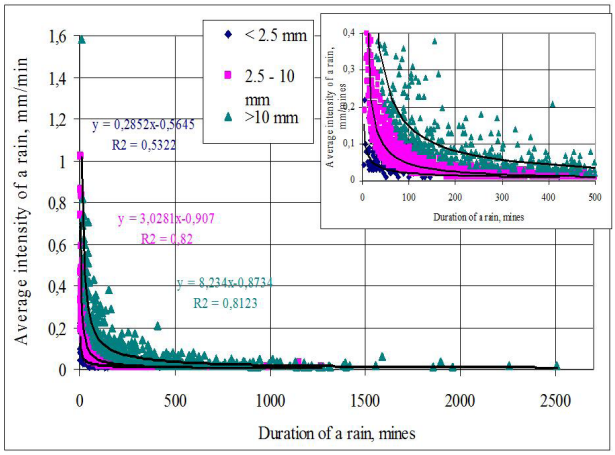

Figure 3. Dependence of the average intensity of precipitation on their duration at the Kamenka-Bugskaya meteorological station, differentiated by the amount of precipitation per rain.

Table 4. Probability of occurrence of rains of different intensities, %.

Characteristic	Gradations	Weather station															
		Kyiv				Kamenka-Bugskaya				Kyiv				Kamenka-Bugskaya			
		Average intensity of precipitation, mm/min								Precipitation duration, min							
		0.01	0.04	0.125	0.5	0.01	0.04	0.125	0.5	10	20	60	180	10	20	60	180
The amount of precipitation for rain, mm	< 2.5 mm	52	20	3	-	91	51	4	-	80	65	35	10	93	75	30	2.3
	2.5-10 mm	79	37	11	-	85	50	13	0.5	99.6	97	80	45	99	96	77.7	39
	> 10 mm	95	56	22	1	98	73	26	2.7	-	-	95	72	99.8	98.6	92	62.6
	Whole range	73	35	10	0.5	89	57	16	1	95	88	68	39	99.5	95.9	79.6	44
Precipitation duration for rain, min	< 60 min	92	57	22	1	99.9	96	52	5.5								
	60-180 min	92	52	8	-	99.9	71	13.5	-								
	> 180 min	93	21	1	-	99.9	26	1.7	-								
	Whole range, min	93	42	10	1	99.9	56.5	16.2	1								

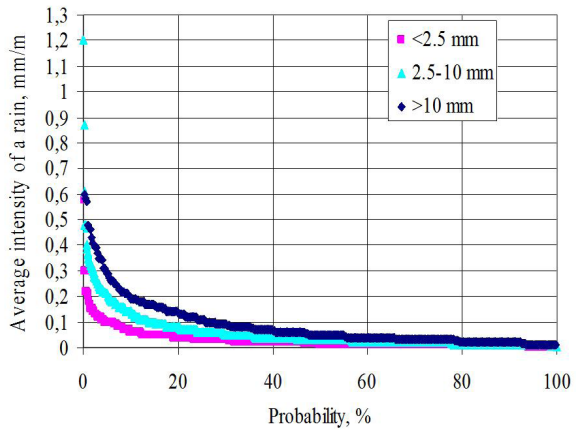

Figure 4. Availability of average intensity of precipitation at the meteorological station Kyiv is differentiated by the amount of precipitation per rain.

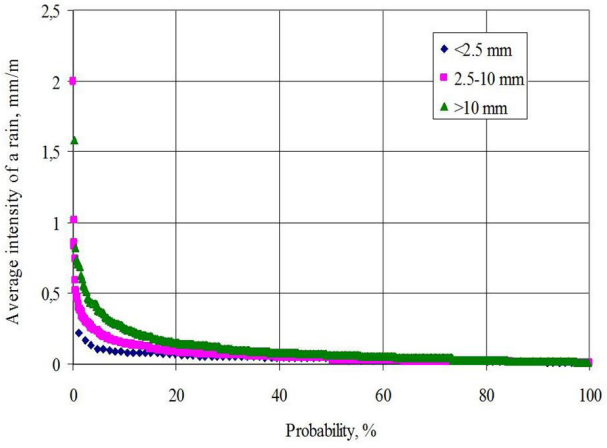

Figure 5. Availability of average precipitation intensity at the weather station Kamenka-Bugskaya is differentiated by the amount of precipitation per rain.

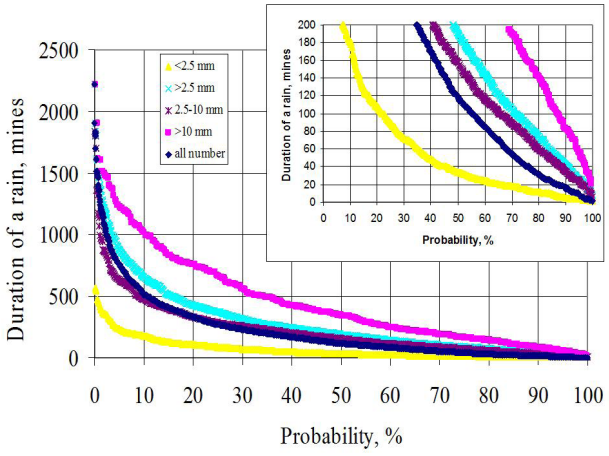

Figure 6. Availability of precipitation duration according to Kyiv weather station differentiated by the amount of precipitation per rain.

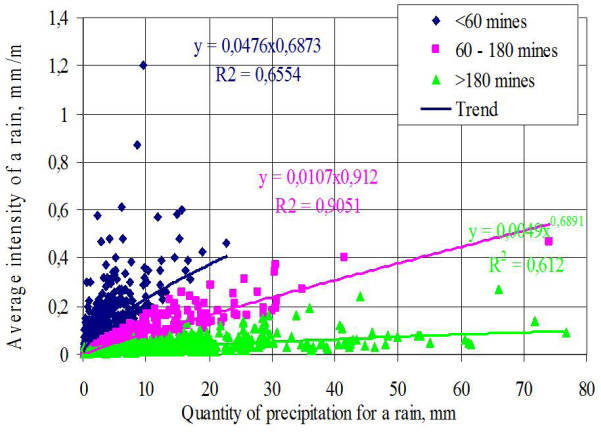

Figure 7. Dependence of the intensity of precipitation on their amount, differentiated by the duration of rain at the meteorological station Kyiv.

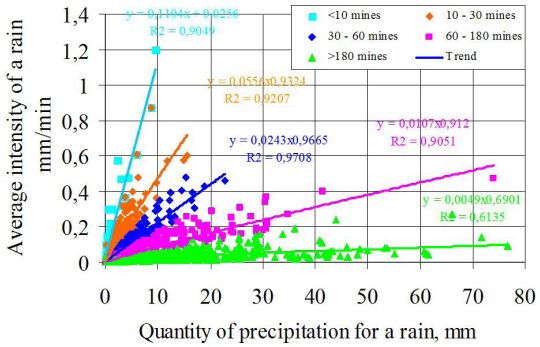

Figure 8. Dependence of the intensity of precipitation on their amount, differentiated in more detail by the duration of the rain, Kyiv meteorological station.

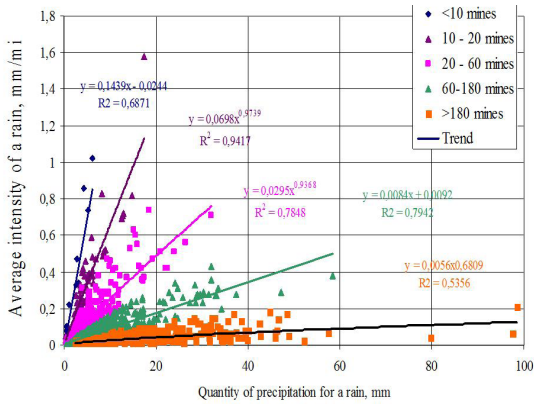

Figure 9. Dependence of the intensity of precipitation on their amount, differentiated in more detail by the duration of rain, meteorological station Kamenka-Bugskaya.

of rain does not depend on either the amount of precipitation or its duration. The change in the intensity of precipitation presumably depends on the synoptic conditions of their formation, as well as on the power of the process and baric gradients. At the front line, in the presence of a large temperature contrast, the most intense precipitation falls, and with the distance from the frontal section, their intensity weakens [3]. Our studies of the rain [24] show that the position of the intensity maximum during rain depends on the amount of precipitation, its duration and average intensity, air and soil surface temperature, air humidity, and wind speed.

Studies by N.V. Gladun et al. [25] show a large weight of precipitation of low intensity in the structure of shower precipitation. The duration of precipitation with an intensity of 0.01-0.10 mm/min is 51% of the duration of the rest of the precipitation, and the area occupied by them is 44% of the area of precipitation of greater intensity.

According to the course of rain intensity Z.P. Bogomazova and Z.P. Petrova [26] identified 6 types of rains.

The probability of the position of the maximum intensity of precipitation during rain for rains with different amounts of precipitation has more significant differences for precipitation less than 2.5 mm (the curves are more curved), for rains of 2.5 mm and more, the probability curves are closer to straight lines (**Figure 10**). Apparently, this is due to the fact that precipitation less than 2.5 mm is more heterogeneous in origin, it can be dew and drizzle, etc.

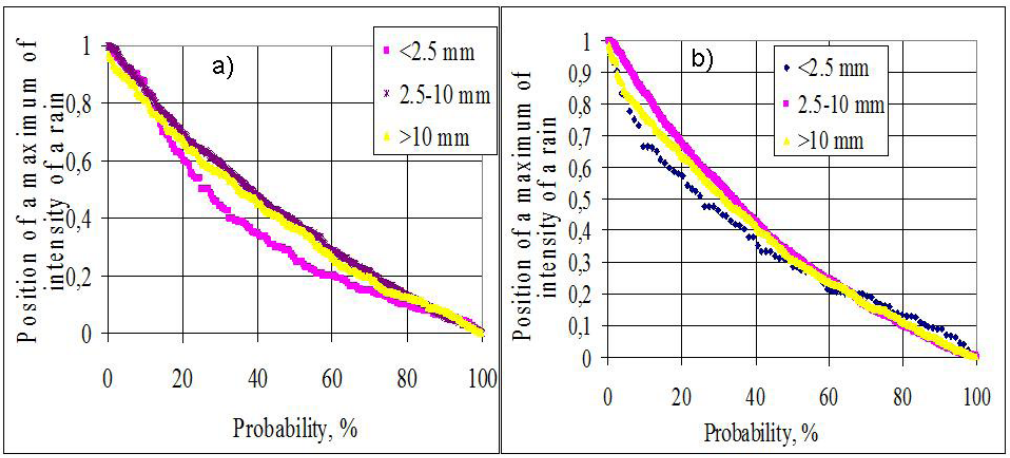

Figure 10. Availability of the position of the maximum intensity of precipitation at meteorological stations Kyiv (a) and Kamenka-Bugskaya (b) differentiated by the amount of precipitation per rain.

When differentiating the probability curves for the position of the maximum intensity of precipitation during rain by the duration of the rain, it is noted that rains of longer duration (more than 180 min) line up more in a straight line than rains of shorter duration (**Figure 11**). Moreover, rains lasting less than 60 minutes show a greater curvature of the probability curve, which is most likely due to the greater heterogeneity of the nature of precipitation in this category, there may be short rains with low precipitation and intense showers.

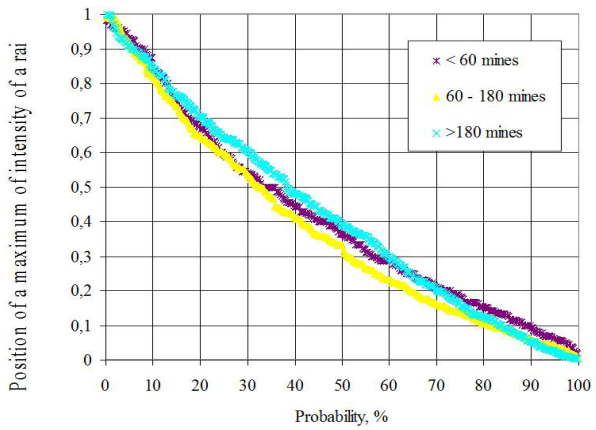

Figure 11. Availability of the position of the maximum intensity of precipitation at the meteorological station Kyiv is differentiated by the duration of precipitation per rain.

4. Discussion and conclusions

The dependence of the average intensity of precipitation on their duration for the entire range of series of observations is not described by a power law with a sufficient degree of reliability, and when differentiated into gradations according to the amount of precipitation (< 2.5 mm, 2.5-10 mm, ≥ 10 mm), the dependences are obtained with a high degree of correlation (**Figures 1 and 3**).

The scatter of points can be explained by the presence of intermediate categories, which does not take into account the accepted division of the data. Thus, for large values of the amount of precipitation, the existence of a separate curve is possible, since the existing classifications of precipitation imply the division of heavy showers into separate gradations (heavy, mountainous, texases, etc. [23]).

Differentiation of rains by their duration shows a stronger stratification of the field of points for shorter rains (up to 60 minutes). This stratification of the field of points is successfully differentiated into shorter segments of 20, 30 minutes. Associated with greater heterogeneity of shorter duration precipitation, it can be both rains of low intensity and heavy downpours of short duration. The deepening of differentiation by the duration of precipitation of shorter rains increases the tightness of the grouping of points near the trend lines.

The probability of the position of the maximum intensity of precipitation during rain for rains with different amounts of precipitation has more significant differences for precipitation less than 2.5 mm (the curves are more curved), for rains of 2.5 mm and more, the probability curves are closer to straight lines, which is associated with a greater rainfall heterogeneity less than 2.5 mm.

The conducted studies show the possibility of creating a classification of atmospheric precipitation based on the quantitative principle. Why is it necessary to increase the spatial coverage of the territory and introduce into consideration the characteristics of the state of the weather at the time of precipitation (air temperature, atmospheric pressure, wind speed, etc.).

Conflict of Interest

The author has no conflict of interest.

Data Availability Statement

Work is executed on materials of supervision to the state hydrometeorological service for the long-term period. The part of materials is published in Meteorological monthly journals and Materials of supervision [15,19,20]. They are accessible in the central libraries of the countries of the former USSR and Ukraine including. The part is accessible in the state archive of the hydrometeorological service of Ukraine (these are materials with 1995 for 2020 and supervision over rains with the quantity of precipitations less than 10 mm).

References

[1] Линслей, Р.К., Колер, М.А., Паулюс, Д.Л.Х., 1962. Прикладная гидрология (Russian) [Applied hydrology]. Гидрометиздат: Ленинград. pp. 759.

[2] Соколовский, Д.Л., 1959. Речной сток (основы теории и практики расчетов) (Russian) [River flow (basics of theory and practice of calculations)]. Гидрометеорологическое издательство: Ленинград. pp. 527.

[3] Алибегова, Ж.Д., 1985. Пространственно-временная структура полей жидких осадков (Russian) [Spatio-temporal structure of liquid precipitation fields]. Гидрометиздат: Ленинград. pp. 229.

[4] Llasat, M.C., 2001. An objective classification of rainfall events on the basis of their convective features: Application to rainfall intensity in the northeast of Spain. International Journal of Climatology: A Journal of the Royal Meteorological Society. 21(11), 1385-1400.

[5] Соколовский, Д.Л., 1952. Речной сток (основы теории и практики расчетов) (Russian) [River flow (basics of theory and practice of calculations)]. Гидрометеорологическое издательство: Ленинград. pp. 492.

[6] Берг, Э.Ю., 1925. Данные о наиболее выдающихся ливневых дождях разной продолжительности за десятилетие 1903-1912 гг. на территории бывшей Европейской России (Russian) [Data on the most outstanding rain showers of various durations for the decade 1903-1912. on the territory of the former European Russia]. Географический сборник: Ленинград.

[7] Чеботарев, Н.П., 1939. Сток и гидрологические расчеты (Russian) [Stock and hydrological calculations]. Гидрометеорологическое издательство: Москва. pp. 319.

[8] Maynard, B., 2006. Meteorological Information in Support of De-ising and Anti-icing Operations [Internet]. Available from: https://www.icao.int/safety/meteorology/amofsg/AMOFSG%2016%20Archive%20Material/AMOSSG%206/SNs/AMOSSG.6.SN.010.5.en.doc

[9] World Meteorological Organization, 2018. Guide to instruments and methods of observation. World Meteorological Organization: Geneva, Switzerland. pp. 548.

[10] Ramli, S., Bakar, S.H.A., Tahir, W. (editors), 2011. Radar hydrology: New Z/R relationships for Klang River Basin, Malaysia based on rainfall classification. 2011 IEEE Colloquium on Humanities, Science and Engineering; 2011 Dec 5-6; Penang, Malaysia. New York: IEEE. p. 537-541.

[11] Мисюра, Л.И., 1969. Справочник по климату СССР., Вып.10. Украинская СССР. Ч. IV. Влажность воздуха, атмосферные осадки и снежный покров (Rrussian) [Reference book on the climate of the USSR. Issue 10. Ukrainian USSR. Part IV. Humidity, atmospheric precipitation and snow cover]. Ленинград: Гидрометиздат. pp. 1-696.

[12] Прокофьев, О.М., 2015. Сезонный ход количества крупномасштабных и конвективных осадков (Russian and Ukranian) [Seasonal change in the amount of large-scale and convective precipitation]. Вісник ОНУ. Сер.: Географічні та геологічні науки. 20(2), 35-47.

[13] Budnik, S.V., 2019. Change of erosive activity in the context of change of the climate. Climate change impacts on hydrological processes and sediment dynamics: Measurement, modelling and management. Springer: Cham. pp. 16-28. DOI: https://doi.org/10.1007/978-3-030-03646-1_4

[14] Budnik, S.V., 2019. Spatio-temporal change of atmospheric precipitation on territory of North-West of Ukraine. Journal of Atmospheric Science Research. 2(4), 1-4. DOI: https://doi.org/10.30564/jasr.v2i4.1564

[15] Мисюра, Л.И., 1962. Метеорологические данные за отдельные годы. Вып.10. По Украинской ССР. Ливневые дожди и суточные количества осадков за 1936-1959 гг. Том 2. Ливневые дожди (Russian) [Meteorological data for selected years. Issue 10. across the Ukrainian SSR. Heavy rains and daily precipitation for 1936-1959 Volume 2.

Heavy rains.] Под ред. Л.И.Мисюры. Ленинград: Гидрометеорологическое издательство. pp. 1-384.

[16] Инструкция для наблюдений над атмосферными осадками. 1896; 1897; 1899; 1902; 1903; 1909; 1910; 1911; 1914 (ГФО), 1930 – ГМК СССР. ГГО; 1934 – ЦУЕГМС СССР. ГГО. С.Пб – Петроград – Ленинград (Russian) [Instructions for observing atmospheric precipitation. 1896; 1897; 1899; 1902; 1903; 1909; 1910; 1911; 1914 (GFO), 1930 - MMC of the USSR. GGO; 1934 - TSUEGMS of the USSR. GGO. S.Pb - Petrograd - Leningrad.]

[17] Кедроливанский, В.Н., 1954. Наставление гидрометеорологическим станциям и постам., Вып.3. Метеорологические наблюдения на станциях. Ч.1. Основные метеорологические наблюдения (Russian) [Instructions for hydrometeorological stations and posts. Issue 3. Meteorological observations at stations. Part 1. Basic meteorological observations. L. GUGMS at the Council of Ministers of the USSR]. Ленинград. ГУГМС при СМ СССР.

[18] Беспалов, Д.П., 1958. Наставление гидромете орологическим станциям и постам., Вып.3. ч.1. Метеорологические наблюдения на станциях (Russian) [Instructions for hydrometeorological stations and posts. Issue 3. part 1. Meteorological observations at stations]. Ленинград. ГУГМС при СССР.

[19] Богомазова, З.П., 1940. Водный кадастр Союза ССР. Ливни на территории СССР (Russian) [Water Cadastre of the USSR. Downpours on the territory of the USSR]. Под ред. Ленинград-Москва: Гидрометеорологическое издательство. pp. 1-431.

[20] Метеорологический ежемесячник. 1961-2020. Вып.10. Украина. Ч2. Киев. 1961-2020 гг (Russian and Ukrainian) [Meteorological monthly. Issue 10. Ukraine. Ch2. Kyiv. 1961-2020].

[21] Великанов, М.А., 1940. Водный баланс суши (Russian) [Water balance of the land]. Гидрометеорологическое издательство: Москва. pp. 182.

[22] Григорьева, Л.К., 1957. Исследование ливней на территории Велико-Анадольского ливнемерного куста (Russian) [Investigation of showers on the territory of the Veliko-Anadol storm-measuring bush]. Труды Укр. НИГМИ. - Вып. 9, 149-155.

[23] Горбачев, П.Ф., 1925. О предельных силах ливней (Russian) [On the limiting forces of showers]. Труды Первого Всероссийского гидрологического съезда. Ленинград. 379-381.

[24] Будник, С.В., 2007. Ливневый сток со склонов (Russian) [Storm runoff from the slopes]. Житомир. ЖГУ им. И. Франко. 184.

[25] Гладун, Н.В., Корниенко, Е.Е., Ченакал, Ж.И., 1976. О структуре поля интенсивности летних осадков (Russian) [On the structure of the intensity field of summer precipitation]. Труды Укр. НИГМИ. Вып. 146, 79-90.

[26] Богомазова, З.П., Петрова, З.П., 1948. Исследов ание выдающихся дождей на территории УССР их хода и распределения по площади (Russian) [Study of outstanding rains on the territory of the Ukrainian SSR, their course and distribution over the area]. Труды ГГИ. Вып. 6(60), 104-139.

BILINGUAL PUBLISHING GROUP

Journal of Atmospheric Science Research

https://journals.bilpubgroup.com/index.php/jasr

ARTICLE

Air Pollution Risk Assessment Using GIS and Remotely Sensed Data in Kirkuk City, Iraq

***Huda Jamal Jumaah*[1*], *Abed Jasim*[2], *Aydin Rashid*[2], *Qayssar Ajaj*[2]**

[1] *Environment and Pollution Engineering Department, Technical Engineering College of Kirkuk, Northern Technical University, Kirkuk, 36001, Iraq*

[2] *Department of Surveying Engineering, Technical Engineering College of Kirkuk, Northern Technical University, Kirkuk, 36001, Iraq*

ABSTRACT

According to World Health Organization (WHO) estimates and based on a world population review, Iraq ranks tenth among the most air-polluted countries in the world. In this study, the authors tried to evaluate the outdoor air of Kirkuk City north of Iraq. The authors relied on two types of data: field measurements and remotely sensed data. Fifteen air quality points were determined in the study region representing the monthly average measurements implemented for the one-year dataset. Geographic information systems (GIS) based geo-statistic and geo-processing techniques have been applied to collected data. Spatial distribution data related to Air Quality Index (AQI), and Particulate Matter (PM10 and PM2.5) were obtained by mapping collected records. Remotely sensed data of PM2.5 were analyzed and compared with the collected data. Health impacts were assessed per each air pollutant determined in the study. Spatial distribution maps revealed the hazardous air type in the study area. Overall AQI ranged between 300 and 472 μg/m^3 referring to unhealthy, very unhealthy, and hazardous classes of pollution. Also, PM10 ranged between 300 and 570 μg/m^3 indicating the same class of air pollution from unhealthy to hazardous. While PM2.5 ranged between 40 and 60 μg/m^3 which represents unhealthy air for sensitive persons and unhealthy air. The remotely sensed data revealed different air types for the study period ranging from 14.5 to 52.5 μg/m^3 represented in moderate and unhealthy air for sensitive persons. Significant correlations were obtained where the mean local R^2 (coefficient of determination) was obtained as 0.83. The assessed data were within high air pollution that requires immediate intervention for controlling causes and eliminating their effects.

Keywords: Air pollution risk; AQI; GIS; Particulate matter; Remote sensing

*CORRESPONDING AUTHOR:

Huda Jamal Jumaah, Environment and Pollution Engineering Department, Technical Engineering College of Kirkuk, Northern Technical University, Kirkuk, 36001, Iraq; Email: huda80@ntu.edu.iq

ARTICLE INFO

Received: 7 July 2023 | Revised: 15 August 2023 | Accepted: 22 August 2023 | Published Online: 23 August 2023

DOI: https://doi.org/10.30564/jasr.v6i3.5834

CITATION

Jumaah, H.J., Jasim, A., Rashid, A., et al., 2023. Air Pollution Risk Assessment Using GIS and Remotely Sensed Data in Kirkuk City, Iraq. Journal of Atmospheric Science Research. 6(3): 41-51. DOI: https://doi.org/10.30564/jasr.v6i3.5834

1. Introduction

Iraq is known as an oil exporting country and this industry is considered the main source of pollution in Iraq [1,2]. Besides, the country has suffered from many wars that led to many effects including high rates of air pollution [3]. Also, it today suffers from increased daily dust storms [4]. Dust storms cross the borders of countries and increase their intensity and frequency by increasing desertification and reducing vegetation cover. They have adverse effects that carry particles suspended in the air for a long time and cause health effects [5]. The entire world is going through major climate change, including the Middle East region in which Iraq is located [2]. Besides the rapid urbanization and industrialization development combined with the increased number of cars in the streets, have led to serious air contamination in terms of haze. This increased the particulate matter in the air more than standard levels [6]. All these conditions have caused many problems in the country involving high levels of air contamination dramatically [2,3]. Various forms of air pollution are available, but most of them include particulate matter PM2.5 and PM10. PM2.5 particularly, has been detected to be harmful to people according to many epidemiological studies. So, researchers emphasized PM2.5 in air quality evaluation and monitoring [7]. The outcomes of many research show the exceeding levels of these pollutants in various regions in Iraq which passes standard criteria [3,8], where according to an exploratory analysis using a GIS-based spatial method applied in Kirkuk City, defined the high concentrations of PM2.5 as unhealthy air [9].

The U.S. Environmental Protection Agency introduced the AQI which is a useful reporting index of daily air criteria. It reports the air quality data per its health effects [10].

Numerous studies have highlighted the adverse effects of air pollution on public health and the environment [11-13]. However, conducting a comprehensive air pollution risk assessment that incorporates spatial analysis and remote sensing techniques can provide a more detailed understanding of pollution sources, dispersion patterns, and potential exposure hotspots. GIS enables the integration of diverse data layers, including meteorological, topographical, and land-use data, to create accurate pollution models and visualizations [14]. Meanwhile, remotely sensed data acquired from satellites and aerial platforms offer valuable information on pollutant concentrations, atmospheric conditions, and land cover characteristics [15]. By combining these technologies, a holistic approach to air pollution assessment can be achieved [16].

Environmental modeling has a significant history and many applications in environmental-related problems [17]. These problems relate to the study of large areas where the geographic information system (GIS) is a beneficial tool for assessing and evaluating [18].

Whereas, GIS is able to integrate different information sources that allow the interpretation of data via different modeling and visualization techniques [19]. Therefore, GIS is considered a decision support system for the experts concerned with conducting evaluations and management [20-22]. Where using the modeling and GIS-based spatial analysis is risen to date [23]. modern techniques for analyzing, assessing, and modeling have been developed [24]. For instance, air quality assessment is useful in controlling air pollution problems [25]. Geographic information systems (GIS) and remotely sensed data have emerged as invaluable resources for analyzing and visualizing complex environmental phenomena, including air and water pollution [26,27].

In recent years, geographical information systems (GIS) and remotely sensed (RS) data have emerged as valuable tools for analyzing air pollution patterns and assessing associated risks. This study focuses on utilizing GIS and remotely sensed data to conduct an air pollution risk assessment in Kirkuk City, Iraq, a region facing increasing pollution challenges due to rapid urbanization and industrialization.

In the past decade, high levels of air pollution in the city of Kirkuk have become a problem, and have contributed to an increase in the rate of diseases associated with the respiratory system. Most asthma and other respiratory diseases are due to inhaling unclean air, which is polluted and loaded with “toxic gases and smoke emissions” from the oil indus-

try and factories operating in Kirkuk. The city has become the third most polluted city in Iraq. Many causes lie behind the city's air pollution, including the oil industry, vehicle emissions, and waste. It is necessary to assess the risks and aggravation of air pollution in the city. The increasing number of cars in the streets of the city, the large number of private electrical generators, in addition to the industrial development, and the establishment of factories inside or near the city are all factors that have contributed significantly to the high levels of pollution in the air. Nowadays most of Iraq's cities suffering from severe air contamination causing serious health impacts.

This study aimed to investigate the contamination levels in Kirkuk City based on field measurements and remote sensing imagery. Moreover, GIS-based assessment was applied using geo-statistical analysis so health impacts can be determined and hazards of exposure detected. This work can be used for reference to air pollution management.

2. Materials and methods

2.1 Study area

Kirkuk city belongs to Kirkuk province and it's located in the northern part of Iraq. It lies between longitudes (44°14' and 44°28') E and latitudes (35°18' and 35°32') N. **Figure 1** represents the Kirkuk study area of air quality.

The study area climate is described as dry, very hot, and hot semi-arid in the summer season while, is cold in winter with rain periods from October to April, with an average annual precipitation of 342.7 mm. The evapotranspiration ranges about 1662.9 mm with average annual temperatures of 3 °C to 43 °C [28].

2.2 Datasets and measurements

Fifteen air quality points were selected in the study area, each point representing an area in the study site, the city of Kirkuk. The study period extended from April 2022 to January 2023, which was applied in the city of Kirkuk and included all areas within the city limits.

Data were collected in three ways: manually applied field measurements, remote sensing-based data downloaded as satellite imagery, and station data downloaded from global atmospheric sites. Field data have been collected regularly by five daily measurements at each point then we used the average value of all applied monthly measurements.

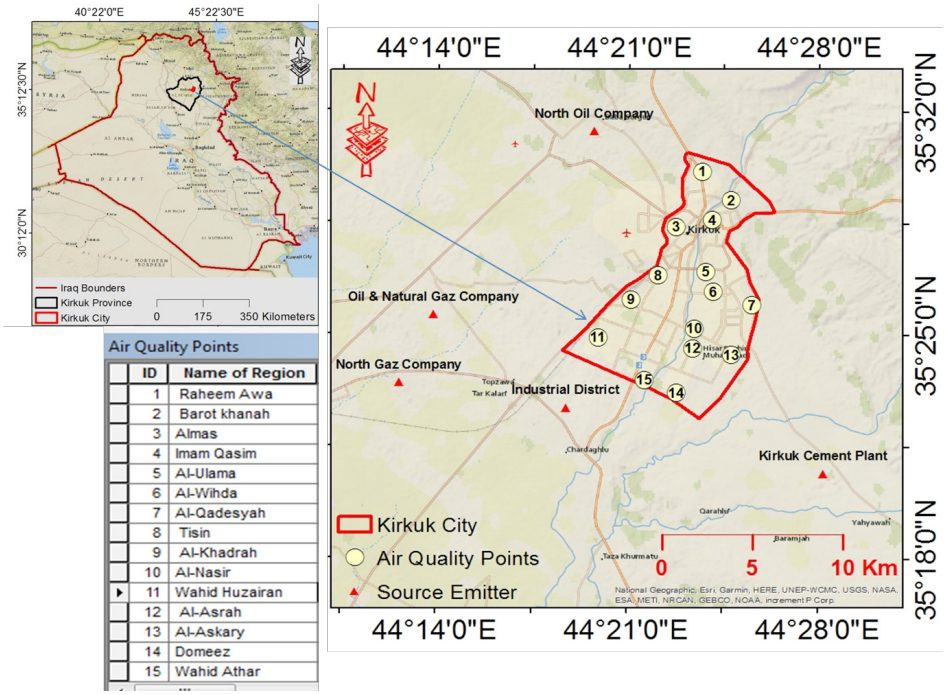

Air Quality Points

ID	Name of Region
1	Raheem Awa
2	Barot khanah
3	Almas
4	Imam Qasim
5	Al-Ulama
6	Al-Wihda
7	Al-Qadesyah
8	Tisin
9	Al-Khadrah
10	Al-Nasir
11	Wahid Huzairan
12	Al-Asrah
13	Al-Askary
14	Domeez
15	Wahid Athar

Figure 1. Kirkuk study area of air quality.

While AQI data were gathered from the historical data of the Kirkuk ground station for each month. The average value was used for mapping. Remotely sensed PM2.5 extracted from specific images for each month.

We relied on manual measurements using an Air Quality Monitor for trained data and Air Quality Multimeter for tested data. Air Quality Monitor (ZH01-B) a portable dust concentration device measures suspended dust particles data of PM10, PM5, PM2.5, and PM1 with a range of 0-1000 μg/m^3, ± 20% accuracy and 1 μg/m^3 resolution. In terms of health effects according to the criteria, we divided the type of data into two parts PM10 and less, and PM2.5 and less. Air Quality Multimeter device was used to collect tested PM2.5 data which was used later for validations. The device measures dust PM2.5 with a range of 0-500 μg/m^3 and ± 10% accuracy.

Remotely sensed PM2.5 data were downloaded from an open-source application via [29]. These data comprise PM2.5 dust mass levels extracted from the M2TMNXAER dataset which is data collection in (MERRA-2) Modern-Era Retrospective analysis for Research and Applications version 2. This group data comprise integrated aerosol diagnostics, for example (dust PM2.5, sulfate, black and organic carbon, aerosol, and Aerosol Optical Thickness (AOT) at 550 nm). In addition, it contains a variance of definite factors. MERRA-2 is the modern ver. of universal atmospheric re-analysis for the satellite era created by NASA Global Modeling and Assimilation Office (GMAO) via the Goddard Earth Observing System Model (GEOS) version 5.12.4.

Moreover, AQI data were obtained from the Air Matter Global Service downloaded from [30]. Air Matter displays air AQI for Kirkuk city station in the study area. We collected the ten months' data and then used the average in our investigation.

2.3 Methods

In this study, two GIS techniques were applied to draw distributed air pollution maps and to predict new locations based on the coordinates of each region and city boundaries of Kirkuk.

GIS-based geo-processing was used for the raster conversion of the downloaded images of each date (April 2022, June 2022, August 2022, October 2022, December 2022, and January 2023). The geo-processing outcomes have resulted in polygon data which was used later for mapping and point data estimation.

Besides, GIS-based geo-statistics has been applied for mapping air pollution distributed maps of the field data. Which was used to interpolate the points by Inverse Distance Weighted (IDW) to predict the new points data based on used 15 air quality points. This was applied to field group PM data.

The applied methods in the study are shown in **Figure 2**. Furthermore, **Table 1** represents the air quality criterion.

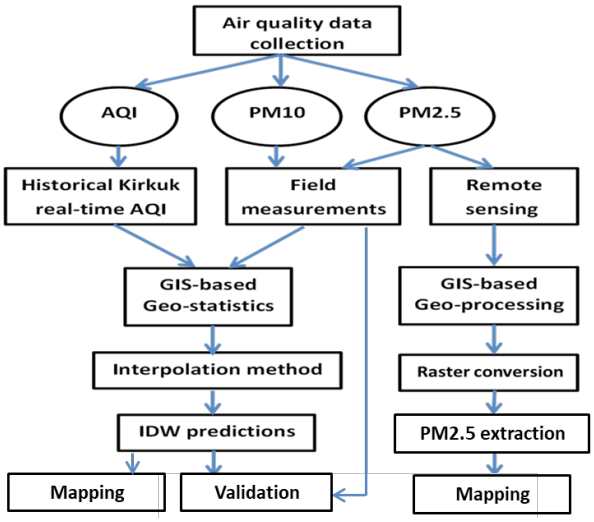

Figure 2. The applied methods in the study.

Table 1. Air quality criterion [3].

AQI	PM2.5 (μg/m^3)	PM10 (μg/m^3)	Air quality
0-50	0-12.0	0-54	Good
51-100	12.1-35.4	55-154	Moderate
101-150	35.5-55.4	155-254	Unhealthy for sensitive groups
151-200	55.5-150.4	255-354	Unhealthy
201-300	150.5-250.4	355-424	Very unhealthy
301-500	250.5-500.4	425-604	Hazardous

Table 1 involves the air quality criteria for AQI, PM2.5, and PM10. Based on these criteria we can describe whether air quality is healthy or not. Air

quality is classified as good, moderate, and unhealthy. Besides the table involve the very unhealthy with hazardous air type and the unhealthy for sensitive people who suffer from respiratory diseases such as allergies and asthma, in addition to the elderly, and people who suffer from chronic diseases or heart diseases.

3. Results

3.1 GIS-based geo-statistics results

Figure 3 represents the air quality spatial distributions in Kirkuk City from April 2022 to January 2023.

Based on **Figure 3(a)** The AQI was within a very unhealthy air class with an average of 386 AQI. Based on **Figure 3(b)** PM10 was within unhealthy air to hazardous with values of 300 to 570 µg/m^3.

Regions 1, 2, 6, 7, 10, and 14 have shown hazardous values of PM10. Regions 3, 4, 5, 8, 9, and 15 have shown unhealthy air of PM10 concentrations. The remaining areas had very unhealthy air in terms of PM10.

Furthermore, PM2.5 values were between 40 and 60 µg/m^3 as shown in **Figure 3(c)** which represents unhealthy air and values out of standards that result in health effects.

Regions 5, 6, 10, 11, and 15 have shown unhealthy air of PM2.5 concentrations. While the rest areas were within 40-55.4 µg/m^3 unhealthy for sensitive groups of people and they should limit outdoor exertion.

The levels of PM2.5 in **Figure 3** showed unhealthy air for sensitive people in all regions except regions 5, 6, 10, 11, and 15 where depicted unhealthy air is situated in the southwestern part of the city and some regions in the center.

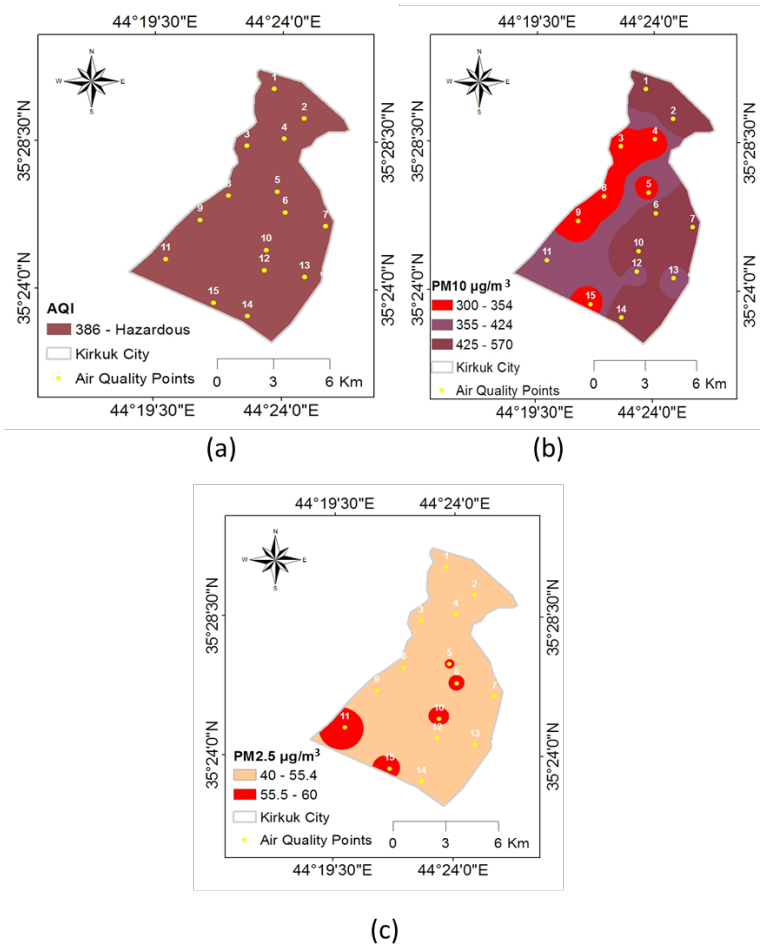

Figure 3. Air quality spatial distributions in Kirkuk city from April 2022 to January 2023: (a) AQI, (b) PM10, (c) PM2.5.

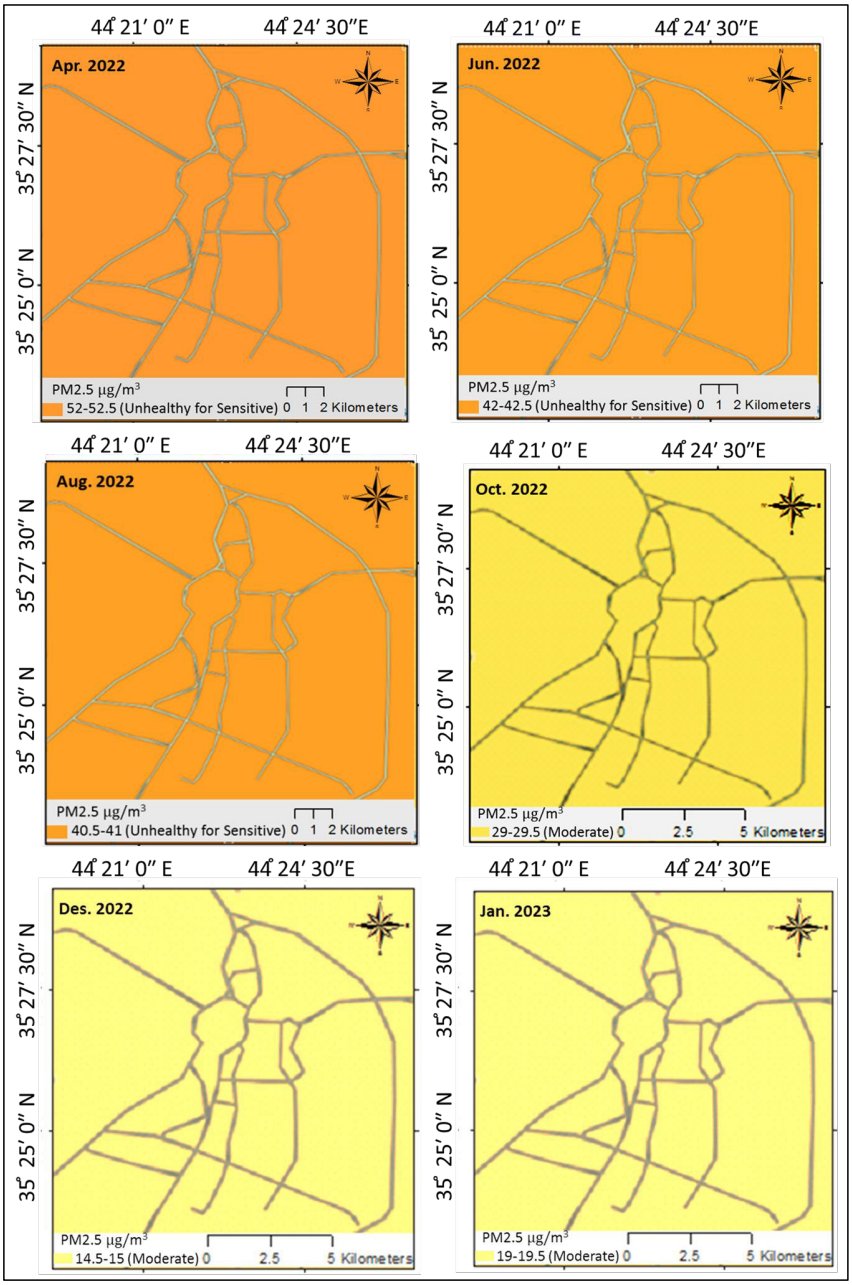

Figure 4. Remotely sensed PM2.5 air quality spatial distributions in Kirkuk city from April 2022 to January 2023.

3.2.GIS-based geoprocessing results

Figure 4 represents the remotely sensed PM2.5 air quality spatial distributions in Kirkuk City from April 2022 to January 2023. PM2.5 values were between 40.5 and 52.5 µg/m^3 for the period of April to August 2022. The air quality was classified as out of criteria that cause some problems for people with respiratory diseases and who have allergies. The highest value was in April 2022 which ranged between 52 and 52.5 µg/m^3. While in June 2022 it ranged between 42 and 42.5 µg/m^3. The lowest value was between 40.5 and 41 µg/m^3 in August 2022.

From October 2022 to January 2023, the air quality was moderate type with no serious effects of PM2.5. The highest values were within 29-29.5 µg/m^3 in October 2022, 14.5 and 15 µg/m^3 in December 2022, and 19-19.5 µg/m^3 in January 2023.

Remotely sensed PM2.5 was at moderate concentrations in the entire Kirkuk in the period of October 2022 to January 2023 as shown in **Figure 4**. While the previous period from April 2022 to August 2022 was unhealthy for sensitive people.

3.3 Validation

In order to validate our data we used Air Quality Multimeter for testing the obtained data based on GIS analysis. Our predictions represented Geo-statistical PM2.5 which was used as trained samples. In order to test and examine obtained predictions tested PM2.5 samples were used which were measured by Air Quality Multimeter in the same 15 regions. **Figure 5** represents the validation of Geo-statistic PM2.5. The obtained R^2 was 0.82 with Root Mean Square (RMS) equal to 51.15 and 1.77 standard deviation.

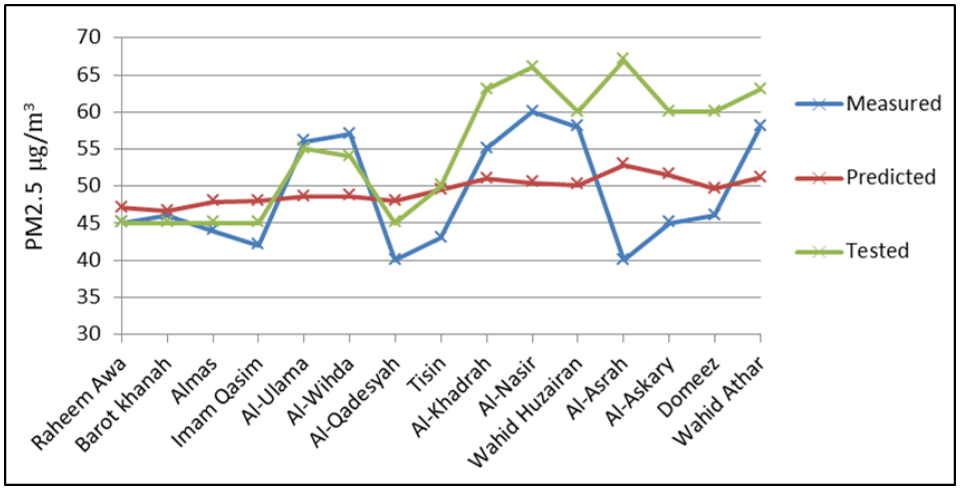

(a)

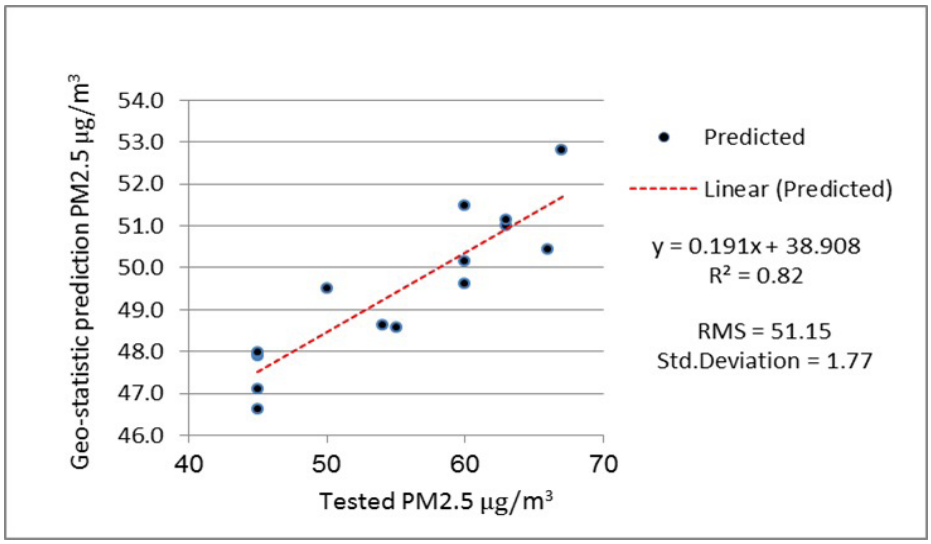

(b)

Figure 5. Validation: (a) PM2.5 dataset (b) Validation of geo-statistic predictions of PM2.5.

4. Discussion

Air contamination is a significant environmental concern that stances numerous risks to public health and ecosystems worldwide. In urban areas, the rapid pace of industrialization, population growth, and urbanization has led to a substantial increase in air pollution levels. Kirkuk City, located in northern Iraq, is no exception, facing similar challenges due to its expanding industrial and urban sectors. To effectively address and mitigate the risks associated with air pollution, it is essential to assess the spatial distribution and identify the contributing factors using advanced tools and techniques.

AQI values were bad in the entire Kirkuk City for the study period. In **Figure 3**, the concentrations of PM10 showed hazardous air in the northern and south-eastern parts. Besides unhealthy to very unhealthy air was depicted in the south-western part of the city and regions 12 and 13.

Based on **Figure 4** also bad air quality was depicted in some periods of the study.

High levels of air pollution and being unhealthy, especially for allergy sufferers, should reduce the time spent outside if symptoms such as difficulty breathing or throat irritation are felt.

Air pollution has exceeded the natural limits and has become outside the national limits, and the green areas are few, compared to the size of the city, and certain areas of industrial activities show an abnormal number of pollution.

Figure 5 the validation applied to the trained data to gain the typical accuracy and to investigate the equivalent range at the measured points using tested points of PM2.5 measured by further devices. The result showed that observations were in the confidence boundary by a high coefficient of determination R^2. This indicates that the predicted values were verified well.

Based on a study [20], GIS-based analysis in Kirkuk City reported an increase in blood disease. Their outcomes conformed to the high incidence of blood disease situated in southern parts of Kirkuk and the minimum spread of blood disease was confirmed in northern parts of Kirkuk and a few areas in the center.

Alongside the obtained results of unhealthy air quality during the study period, a study conducted [9] in Kirkuk province in 2021 resulted in unhealthy air quality, PM2.5 was unhealthy for sensitive people to unhealthy air based on field measurements and remotely sensed images. Developing effective strategies to mitigate and manage air pollution requires accurate assessment and monitoring of pollutant levels.

5. Conclusions

Kirkuk City has witnessed rapid urban growth and industrial activities in recent years. This urbanization process has raised concerns about increasing pollution levels and their potential impacts on the population and environment. However, limited research has been conducted to comprehensively assess air pollution risks in this region. Therefore, this study aims to fill this knowledge gap by utilizing GIS and remotely sensed data to evaluate air pollution risks in Kirkuk City.

In this study, we examined the air quality based on some major air pollutants for risk and evaluation. The concerned data involved the measurement and downloading of air quality parameters such as PM10, PM5, PM2.5, PM1, and AQI. Two GIS-based techniques have been applied for analysis and assessment. The health impacts also were determined for each parameter. Unhealthy to Hazardous air quality was detected in the study area of Kirkuk City. Validation processes resulted in significant value with an accuracy of 82%.

The study recommended monitoring, controlling, and reducing air pollutants values and exposures by methods of alternative strategies and mitigations. Should increase people's awareness of how to deal with the contamination impacts along with early warning and predictions. Besides, promoting clean and renewable energy, and increasing afforestation inside the city to lessen the pollution effect, the future would be more promising. The findings of this research can provide valuable insights for urban planners, policymakers, and environmental agencies

to formulate effective strategies for pollution control and mitigation.

For improving public health, and to a further and wide understanding of the impacts of PM2.5 and PM10 with their toxicological compounds, additional research on sampling regions and results of air pollution should be applied in the study area for further periods.

Author Contributions

H. Jumaah and Q. Ajaj collected the data besides conceptualizing and implementing the analysis; A. Jasim wrote the introduction, A. Rashid discussed the analysis; H. Jumaah edited, updated, and completed writing the paper.

Conflict of Interest

The authors declare that they have no known competing financial interests or personal relationships that could have appeared to influence the work reported in this paper.

Funding

This research received no external funding.

Acknowledgement

The authors acknowledge the use of PM2.5 satellite data from NASA Worldview an open source application. We also acknowledge the use of AQI data from Air Matter a global air quality service site.

References

[1] Al-Hasnawi, S., Hussain, H.M., Al-Ansari, N., et al., 2016. The effect of the industrial activities on air pollution at Baiji and its surrounding areas, Iraq. Engineering. 8(1), 34-44.

[2] Kadhem, J.A., Reza, K.S., Ahmed, W.K., 2017. Alternative fuel use in Iraq: A way to reduce air pollution. European Journal of Engineering and Technology Research. 2(5), 20-30.

[3] Jumaah, H.J., Ameen, M.H., Mahmood, S., et al., 2023. Study of air contamination in Iraq using remotely sensed Data and GIS. Geocarto International. 38(1), 2178518.
DOI: https://doi.org/10.1080/10106049.2023.2178518

[4] Alwaely, A.A., Al-qaralocy, H.N., Al-Asadi, K.A., et al., 2015. The environmental aftermath resulted from chemical bombardment of Halabja Territory for the period 1988-2014. International Journal of Scientific & Engineering Research. 6(9), 40-44.

[5] Alwaeli, A.A., Chaichan, K., Kazem, H.A., 2014. Effect of dust on photovoltaic utilization in Iraq: Review Article. Renewable and Sustainable Energy Reviews. 37, 734-749.

[6] Jumaah, H.J., Kalantar, B., Halin, A.A., et al., 2021. Development of UAV-based PM2.5 monitoring system. Drones. 5(3), 60.
DOI: https://doi.org/10.3390/drones5030060

[7] Ameen, M.H., Jumaah, H.J., Kalantar, B., et al., 2021. Evaluation of PM2. 5 particulate matter and noise pollution in Tikrit University based on GIS and statistical modeling. Sustainability. 13(17), 9571.

[8] Al-Kasser, M.K., 2021. Air pollution in Iraq sources and effects. IOP Conference Series: Earth and Environmental Science. 790(1), 012014.

[9] Hamed, H.H., Jumaah, H.J., Kalantar, B., et al., 2021. Predicting PM2. 5 levels over the north of Iraq using regression analysis and geographical information system (GIS) techniques. Geomatics, Natural Hazards and Risk. 12(1), 1778-1796.
DOI: https://doi.org/10.1080/19475705.2021.1946602

[10] Jumaah, H.J., Ameen, M.H., Kalantar, B., et al., 2019. Air quality index prediction using IDW geostatistical technique and OLS-based GIS technique in Kuala Lumpur, Malaysia. Geomatics, Natural Hazards and Risk. 10(1), 2185-2199.
DOI: https://doi.org/10.1080/19475705.2019.1683084

[11] Wilkinson, P., Smith, K.R., Davies, M., et al.,

2009. Public health benefits of strategies to reduce greenhouse-gas emissions: Household energy. The Lancet. 374(9705), 1917-1929.

[12] Zhang, Q., Zheng, Y., Tong, D., et al., 2019. Drivers of improved PM2. 5 air quality in China from 2013 to 2017. Proceedings of the National Academy of Sciences. 116(49), 24463-24469.

[13] Jumaah, H.J., Mansor, S., Pradhan, B., et al., 2018. UAV-based PM2.5 monitoring for small-scale urban areas. International Journal of Geoinformatics. 14(4), 61-69.

[14] Mahmood, M.R., Jumaah, H.J., 2023. NBR index-based fire detection using Sentinel-2 images and GIS: A case study in Mosul Park, Iraq. International Journal of Geoinformatics. 19(3), 67-74.
DOI: https://doi.org/10.52939/ijg.v19i3.2607

[15] Najim, A.O., Meteab, M.A., Jasim, A.T., et al., 2023. Spatial analysis of particulate matter (PM10) using MODIS aerosol optical thickness observations and GIS over East Malaysia. The Egyptian Journal of Remote Sensing and Space Science. 26(2), 265-271.

[16] Jumaah, H.J., Abbas, W.H., Khalaf, Z.A., et al., 2023. Applications of remote sensing and GIS in assessing climate change and forecasting air quality in Iraq. Journal of Engineering and Technology Development. 1(1), 1-7.
DOI: https://doi.org/10.56391/JETD.2023.1002

[17] Fedra, K., 1993. GIS and Environmental Modeling [Internet]. [cited 2023 May 10]. Available from: http://pure.iiasa.ac.at/id/eprint/3730/1/RR-94-02.pdf

[18] Yi, X., Zhang, J., Wang, Z., et al. (editors), 2018. Deep distributed fusion network for air quality prediction. Proceedings of the 24th ACM SIGKDD International Conference on Knowledge Discovery & Data Mining; 2018 Aug 19-23; London, UK. p. 965-973.

[19] Kalantar, B., Ueda, N., Al-Najjar, H.A.H., et al., 2019. UAV and Lidar image registration: A SURF-based approach for ground control points selection. The International Archives of the Photogrammetry, Remote Sensing and Spatial Information Sciences. 42, 413-418.
DOI: https://doi.org/10.5194/isprs-archives-XLII-2-W13-413-2019

[20] Ajaj, Q.M., Shareef, M.A., Hassan, N.D., et al., 2018. GIS based spatial modeling to mapping and estimation relative risk of different diseases using inverse distance weighting (IDW) interpolation algorithm and evidential belief function (EBF) (Case study: Minor Part of Kirkuk City, Iraq). International Journal of Engineering & Technology. 7, 185-191.

[21] Jumaah, H.J., Kalantar, B., Ueda, N., et al. (editors), 2021. The Effect of war on land use dynamics in Mosul Iraq using remote sensing and GIS techniques. 2021 IEEE International Geoscience and Remote Sensing Symposium IGARSS; 2021 Jul 11-16; Brussels, Belgium. New York: IEEE. p. 6476-6479.

[22] Kalantar, B., Ameen, M.H., Jumaah, H.J., et al., 2020. Zab River (IRAQ) sinuosity and meandering analysis based on the remote sensing data. The International Archives of the Photogrammetry, Remote Sensing and Spatial Information Sciences. 43, 91-95.
DOI: https://doi.org/10.5194/isprs-archives-XLIII-B3-2020-91-2020

[23] Jumaah, H.J., Ameen, M.H., Kalantar, B., 2023. Surface water changes and water depletion of Lake Hamrin, Eastern Iraq, using Sentinel-2 images and geographic information systems. Advances in Environmental and Engineering Research. 4(1), 1-11.

[24] Stillwell, J., Clarke, G., 2004. Applied GIS and spatial analysis. Wiley: Chichester. pp. 254-255.

[25] Hossain, E., Shariff, M.A.U., Hossain, M.S., et al., 2020. A novel deep learning approach to predict air quality index. Advances in Intelligent Systems and Computing. Springer: Singapore. pp. 367-381.

[26] Habbeb, M.G., Sulyman, M.H., Jumaah, H.J., 2022. Modeling water quality index using geographic information systems and weighted arithmetic index in Kirkuk, Iraq. Pollution Research. 41(1), 323-327.

[27] Jumaah, H.J., Ameen, M.H., Mohamed, G.H., et al., 2022. Monitoring and evaluation Al-Razzaza lake changes in Iraq using GIS and remote sensing technology. The Egyptian Journal of Remote Sensing and Space Science. 25(1), 313-321. DOI: https://doi.org/10.1016/j.ejrs.2022.01.013

[28] Hadi, A.M., Mohammed, A.K., Jumaah, H.J., et al., 2022. GIS-based rainfall analysis using remotely sensed data in Kirkuk Province, Iraq: Rainfall analysis. Tikrit Journal of Engineering Sciences. 29(4), 48-55.

[29] EOSDIS Worldview, 2013. NASA EOSDIS [Internet] [cited 2023 Jul 15]. Available from: https://worldview.earthdata.nasa.gov/?v=-1.6482160931174121,-46.54687500000001,202.1794660931174,53.01562500000001&lg=false&t=2023-07-06-T05%3A00%3A53Z

[30] Kirkuk Governorate Real-time Air Quality Index (AQI) & Pollution Report [Internet]. Air Matters. [cited 2023 Jul 15]. Available from: https://air-quality.com/place/iraq/kirkuk-governorate/1edc7885?lang=en&standard=aqi_us

BILINGUAL PUBLISHING GROUP
Tel:+65 65881289
E-mail: contact@bilpublishing.com
Website:https://journals.bilpubgroup.com

2630-5119 03
9 772630 511232